AG-336



# 8. WALL CORRECTION METHODS FOR V/STOL CONFIGURATIONS, HELICOPTERS, PROPELLERS AND WINDMILLS

AUTHOR : J.E. HACKETT

PAGE

# 8 WALL CORRECTION METHODS FOR V/STOL CONFIGURATIONS, HELICOPTERS, PROPELLERS AND WINDMILLS

## Notation

$A_m$ momentum area of lifting system. (Equation 8.5)

$A_{TUN}$ tunnel cross sectional area. Usually B times H

B total tunnel width

b effective span of powered lifting system (in Souths criterion, Section 8.1.2)

$b_S$ span of line source used for wake modeling (Section 8.3)

$c_S$ X-spacing between solid blockage source and sink (Section 8.3)

$C_L$ lift coefficient, L / q S

$C_D$ drag coefficient, D / q S

$C_{D_{VIS}}$ viscous part of model drag coefficient (Section 8.3).

$\Delta C_D$ wake-induced drag increment (see Section 8.3.1).

$C_{Lhb}$ lift coefficient based on Reference area h times b (Souths criterion, chapter 1.2)

$C_T$ thrust coefficient, Thrust / q S

$C_\mu$ jet momentum coefficient, (Jet mass flow times $V_j$ ) / q S

$\bar{c}$ mean chord (Figure 8.12)

D total drag

$D_i$ induced drag

H total tunnel height

h model height above tunnel floor (in Souths criterion, Section 8.1.2)

J advance ratio of rotor or propeller. V / $\Omega_R$

L lift

$L_h$ lift at hover

$M_Y$ pitching moment (Figure 8.12)

n the ratio of final induced velocities in the far wake to initial induced velocities at the model (Chapter 8.2.1.9)

q dynamic pressure = ½ $\rho V^2$

Q generic total 3D source strength. ( = span times strength/unit length)

$\pm Q_S$ total 3D source and sink strengths for line elements representing a model's solid blockage (Section 8.3)

$Q_W$ total 3D source strength for line source element representing a model's viscous wake (Section 8.3)

R rotor or propeller radius (in definition of J, above)

S reference area

$T_S$ static thrust (Figure 8.12)

u generic streamwise velocity increment, relative to U .Positive rearward. (Section 8.3)

$u_{ASYMP}$ asymptotic streamwise velocity increment, at the downstream end of the u-signature, relative to U . (Section 8.3).

$u_{SYM}$ height of the symmetric part of the u-component signature, relative to U (Section 8.3).

$u_{WALL}$ increment of streamwise velocity at a tunnel surface, relative to U . (Section 8.3).

$u_0$ mean or momentum-theory value of absolute longitudinal induced velocity at model, positive rearward. (Section 8.2).

U mainstream velocity.

$V_R$ wind tunnel velocity

$V_J$ jet efflux velocity (in definition of Cμ , above)

V resultant velocity (Equation 8.2)

$w_0$ mean or momentum-theory value of vertical induced velocity at model, positive upward.

$w_h$ reference velocity, positive upward (Equation 8.5)

x, y, z tunnel co-ordinates: axial, along right wing and upward

$X_2$
$X_3$
$X_4$ locations of source elements in pressure signature flow model (Section 8.3)

$\Delta X$ half-width of solid blockage signature at half-height (see Figure 8.21).

$\alpha$ angle of attack.

$\Delta\alpha$ tunnel-induced angle of attack.

$\Gamma$ strength of horseshoe vortex in flow model for matrix version of the pressure signature method (Section 8.3.4).

$\delta_{u,L}$ Interference factor for longitudinal interference velocity due to lift

$\delta_{u,D}$ Interference factor for longitudinal interference velocity due to drag

$\delta_{w,L}$ Interference factor for vertical interference velocity due to lift

$\delta_{w,D}$ Interference factor for vertical interference velocity due to drag

$\delta_{US}$ Upper surface flap angle, to wing chord line (Figure 8.5).

$\theta$ wake deflection angle from the horizontal, positive downward (Figure 8.9).

$\chi$ wake skew angle from the downward vertical to the wake momentum centerline, positive rearward (Figure 8.9).

$\chi_e$ effective wake skew angle from the downward vertical to the wake vorticity centerline. Determined from $\chi_e = \frac{1}{2}(\chi + 90)$. (Section 8.2 )

$\rho$ mass density of tunnel air

$\sigma$ ratio of wind tunnel height to width. (Section 8.2)

$\Omega$ angular velocity of rotor or propeller (in definition of J, above)

# 8.1 INTRODUCTION

## 8.1.1 POSSIBLE APPROACHES FOR POWERED FLOWS

The spectrum of V/STOL configurations that has appeared over the years is very extensive (see Figures 8.1 and 8.2). VTOL configurations may include direct-lift jets, lifting fans, tilt-propellers, tilt-rotors and helicopters. STOL configurations may include wings with highly-deflected flaps or some form of jet-flap, possibly in combination with direct lift. V/STOL systems are thus very diverse and each has its own peculiarities and needs.

The requirements of powered lift testing at low speed are different from those of cruise flight. In the eventual data analyses, the primary interest in tunnel speed corrections is likely to arise from intake momentum drag, for jets or ducted rotors, or advance ratio for open rotors and propellers. Aircraft control is critical in low speed transitional flight and tunnel-induced gradients can be high under these conditions. The gradients, rather than the magnitude, of a correction may determine the correctability of a particular data point. Free stream speed is usually used in normalising powered-flow coefficients such as advance ratio, J, for a rotor; momentum coefficient, $C_\mu$ , for a jet flap or thrust coefficient, $C_T$ , for a direct thrust device. On-line blockage correction is desirable so that constant corrected speed can be maintained at the model reference point. The power coefficient or advance ratio can then be held constant as angle-of-attack, for example, is varied. Provision of on-line blockage corrections is a challenge because of the complexity of the corrections involved.

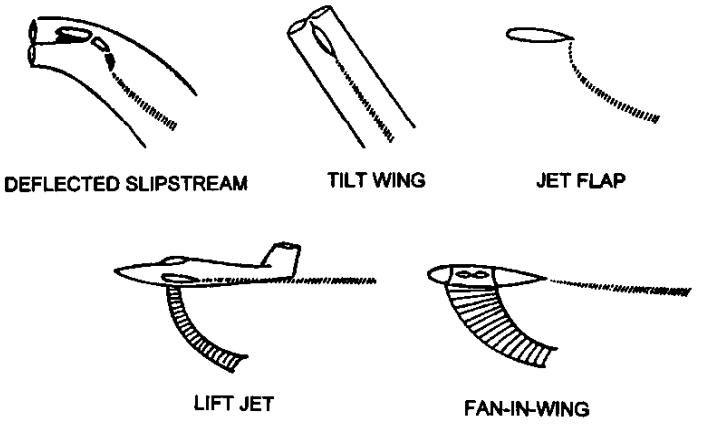


Figure 8.1 Sketches of various V/STOL configurations

For the configurations then in vogue, early work showed that classical tunnel correction methods would suffice provided the test model was aerodynamically small, i.e. on the basis of $C_D$ or $C_L$ times reference area, for example, as opposed to reference area itself. Recognition of this in the fifties and sixties spawned a generation of large V/STOL tunnels and explicit powered flow modelling became an essential part of the correction process. This approach presents significant difficulties because powered, lifting flows generate complex flow structures that change with forward speed. At low speed, impingement on tunnel surfaces is not uncommon. One of the earliest attempts at modelling (Heyson [22]) involved a simple representation of a lifting plume using an inclined line of doublets extending from a jet

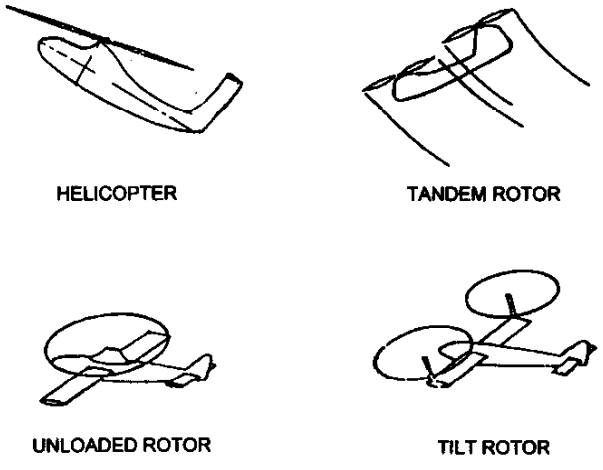


Figure 8.2 Sketches of various open-rotor VSTOL configurations

exit or the centre of a rotor (see Section 8.2). Later, the wall-pressure signature method was developed (See Hackett et al [5], [6] and Section 8.3) and applied with some success to jet flapped wings at very high lift levels ($C_L$>20) and to round lifting jets. The tangential velocities, deduced from measured wall pressures at the centrelines of tunnel surfaces, were applied as boundary conditions in the theoretical flow model. The zero normal flow condition was imposed for the entire solid tunnel surface. Using tunnel wall measurements thus took some of the guesswork out of modelling V/STOL flows. The approach was augmented by the use of local flow control when a jet or a slipstream impinged upon the tunnel floor. This delayed the onset of tunnel flow breakdown significantly. Despite these advances, simple modelling was still required when using the pressure signature method and the numerics could be troublesome. With the recently available two-variable pressure-based correction method (Section 4), it is theoretically possible to avoid explicit modelling for non-impinging flows. However, only explicit modelling can reconstruct the "missing" extension of a powered wake that impacts a tunnel floor.

Methods currently in use cover the spectrum just described. Classical methods, Heyson's model, pressure signature and two-variable methods, and various empirically-based methods are all still in use. There is understandable reluctance to move from familiar methods with a substantial data base to more recent approaches that may require more tunnel time, more instrumentation or both. However, economic pressures are likely to reduce the size of new tunnels and the importance of good correction methods is increasing.

### 8.1.2 THE V/STOL TESTING ENVIRONMENT

A wide variety of installed power systems distinguishes V/STOL models from their conventional counterparts. As indicated in Figures 8.1 and 8.2, these range from shaft- driven rotors to air-powered fans, to jets and various powered wings. Despite this diversity, the test problems of these systems tend to be remarkably similar. Figure 8.3, taken from Tyler et al [41], [42], sketches the flow that arises when a jet impinges on a wind tunnel floor. There is forward flow ahead of the impingement point and, as this flow loses energy, it separates and forms a standing vortex at the tunnel centreplane. This wraps around the impingement region, forming what is sometimes called a "scarf" vortex as its ends trail downstream. The trailing vortices diverge under the influence of their images in the tunnel floor and may progress up the tunnel walls if the conditions are suitable. A similar flow pattern, differing in scale but with the same topology, may be generated by the slipstream from a rotor, a ducted fan or a jet-flapped wing. The term "tunnel flow breakdown" is applied to situations in which data become uncorrectable because of this phenomenon.

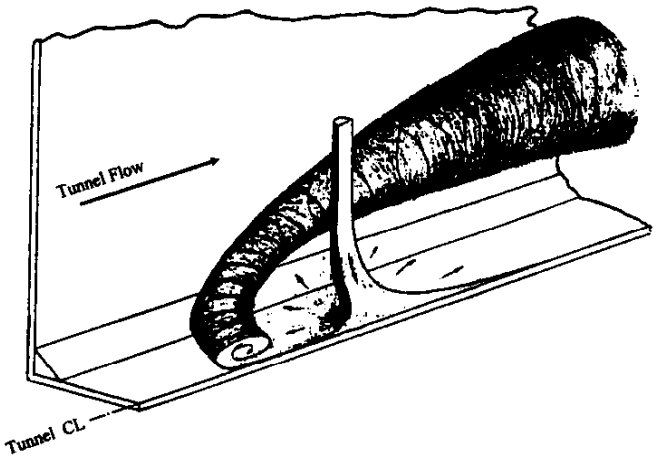


Figure 8.3 Tunnel Flow Breakdown for an Impinging Jet

The tunnel flow breakdown phenomenon is a distinguishing feature of powered flow testing; it rarely occurs with conventional models. It restricts the available test range at low speed and possibly under transitional conditions. For this reason, we shall review the phenomenon in some detail and suggest ways to extend the test envelope by floor blowing.

### 8.1.2.1 TUNNEL FLOW BREAKDOWN CRITERIA

South [40] describes experiments that determine limiting conditions for tunnel flow breakdown. Figure 8.4 shows the resulting criterion and compares it with similar work by Heyson [32]. The ordinate, $C_{Lhb}$ , is a lift coefficient based on the likely tunnel area blocked by the impinging flow, usually expressed as the product of the powered span and the model height. The abscissa is drag-to-lift ratio. It will be observed that South's criterion is more restrictive than Heyson's under thrust conditions.

It is obviously important to monitor the tunnel floor flow in any powered lift test in which South's $C_{Lhb}$ criterion might be exceeded. The use of floor tufts or, better yet, measurement of floor pressures is recommended. Once tunnel flow breakdown occurs in a conventional tunnel the results should be disregarded or at least viewed sceptically. However, the possibility of removing the ground vortex, or at least controlling it, should also be considered. This possibility was investigated, with some success, by Hackett et al [15]. They describe 'worst-case' experiments that employ ground-blowing to delay tunnel flow breakdown.

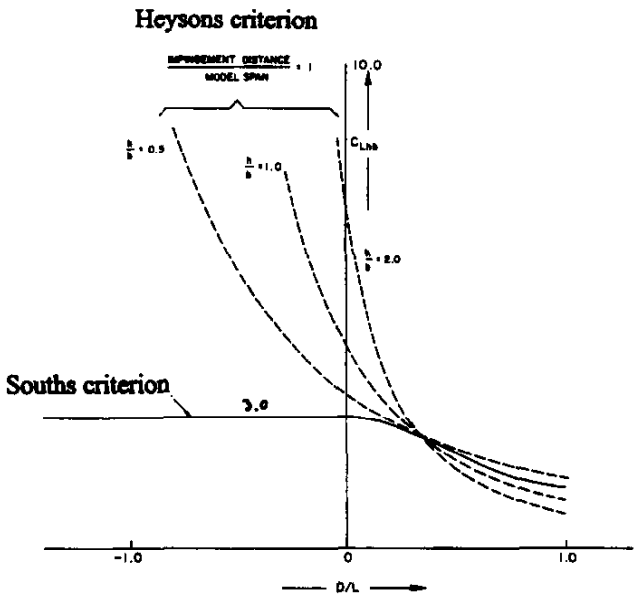


Figure 8.4 Criteria for Tunnel Flow Breakdown

### 8.1.2.2 USE OF FLOOR-BLOWING

Figure 8.5(a), taken from Hackett et al [15], shows laser velocimeter measurements at the centre plane of a finite-span knee-blown flapped wing at a high blowing level. The combined model attitude and flap angle gave a near-vertical jet and a large ground vortex developed which grew as angle-of-attack was increased. Flow beneath the model was effectively blocked, resulting in a loss of lift. Ground blowing was applied to suppress the vortex, using floor pressure measurements to determine the blowing level. The injection point is shown in the figure. With ground blowing set "correctly" (see below), the flow pattern of Figure 8.5(b) was obtained. A ground vortex was still present but its size had been reduced substantially. Inspection of the wing flow reveals increased upper surface velocities, suggesting reduced lift loss.

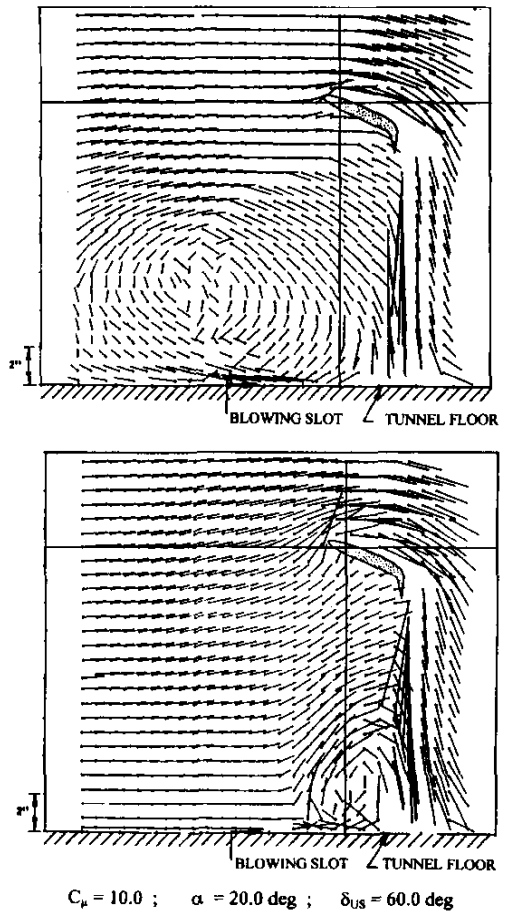


Figure 8.5 Velocity Field at the Centre Plane of a Kneeblowing Flap Model, (a) Fixed Ground (Upper Plot), (b) Blown Ground (Lower Plot)

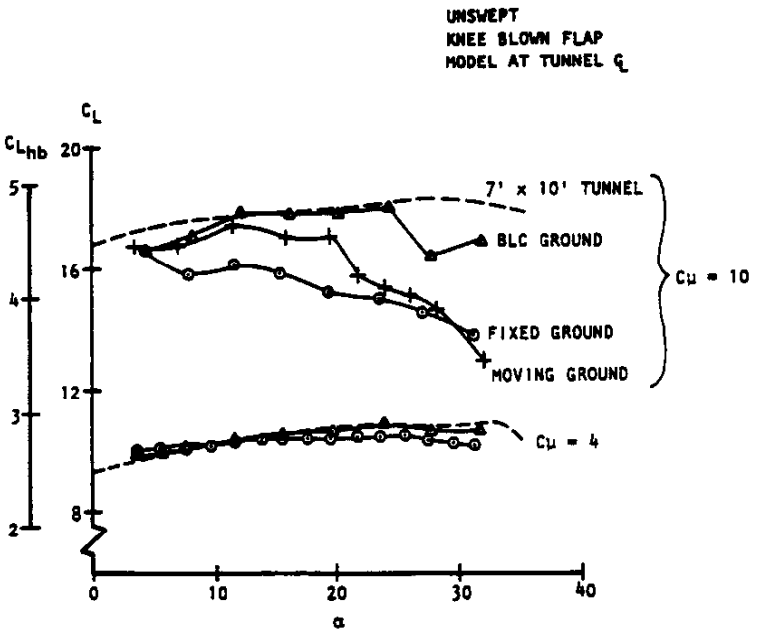


Figure 8.6 Demonstration of Lift-Loss due to Tunnel Flow Breakdown

Figure 8.6, from the same reference, shows the effects of ground flow control on lift. The test was run at "true-q" using the pressure signature method (see Section 8.3) in an on-line mode. A second scale has been added to the y-axis, showing South's tunnel flow breakdown parameter, $C_{Lhb}$. It is evident that the test values for $C_\mu$ = 10 lie well above South's flow breakdown limit. Severe lift loss is apparent for the fixed ground case (circles) relative to the large-tunnel baseline (dashed lines). The loss increases with angle-of-attack. Use of a moving ground (plus-signs) removed most of the deficit but ground blowing (triangles) was more effective at angles of attack below 20-degrees, where the limit of the air supply was reached.

The difference between the moving and the blown-ground results draws attention to the distinction between model-in-ground and free-air interpretation of similar data. We shall now consider these individually.

### 8.1.2.3 FREE-AIR INTERPRETATION

If free-air data are required, more ground flow control may be needed than for the ground effect cases because the ground vortex must be removed as completely as possible. It has already been noted that the moving ground gave less lift recovery than the blown ground. Tunnel constraint corrections for the free-air case must include a four-wall blockage correction, a four-wall angle-of-attack correction and further corrections to both that compensate for the truncation of the powered wake at the tunnel floor.

### 8.1.2.4 GROUND-EFFECT INTERPRETATION

A moving ground is clearly appropriate for ground effect testing. The ground vortex is then smaller than with a fixed ground but larger than for the (free-air) blown ground case. Ground blowing may also be used for ground effect testing but the criterion for setting blowing level is different. For the free air case blowing was increased as needed to remove the suction peak under the ground vortex. However, it is necessary to monitor skin friction at the ground when doing ground-effect testing (see Hackett et al [7]). Preston tubes are installed at the ground surface and the condition is applied that the flow immediately above the ground must be going in the 'right' direction, i.e., the skin friction must be positive. This approximates the moving ground condition.

Three-wall blockage and three-wall angle-of-attack constraint corrections are required when reducing ground-effects data. The three-wall corrections will, of course, be smaller than the corresponding four-wall corrections: the floor images are "supposed" to be there for the ground-effect case. Replacement of the 'missing' plume extension, below the tunnel floor, is not required for in-ground cases.

### 8.1.2.5 'TRUE-Q' TESTING

To illustrate the importance of on-line blockage correction, effective "uncorrected" lift data have been backed out of the Figure 8.6 data. Figure 8.7 shows the result. The blockage corrections are very large and are much more important than those for angle-of-attack. The changes in $C_L$ are almost completely blockage-driven and similar changes can be expected in $C_\mu$. Each uncorrected point (cross) therefore corresponds to a different $C_\mu$. If testing had been conducted at a nominal $C_\mu$ rather than using on-line blockage correction, cross-plotting would have been needed to obtain lines of constant corrected $C_\mu$. Data quality would have suffered and there would probably have been difficulties in deciding on the proper test ranges for the blowing parameters.

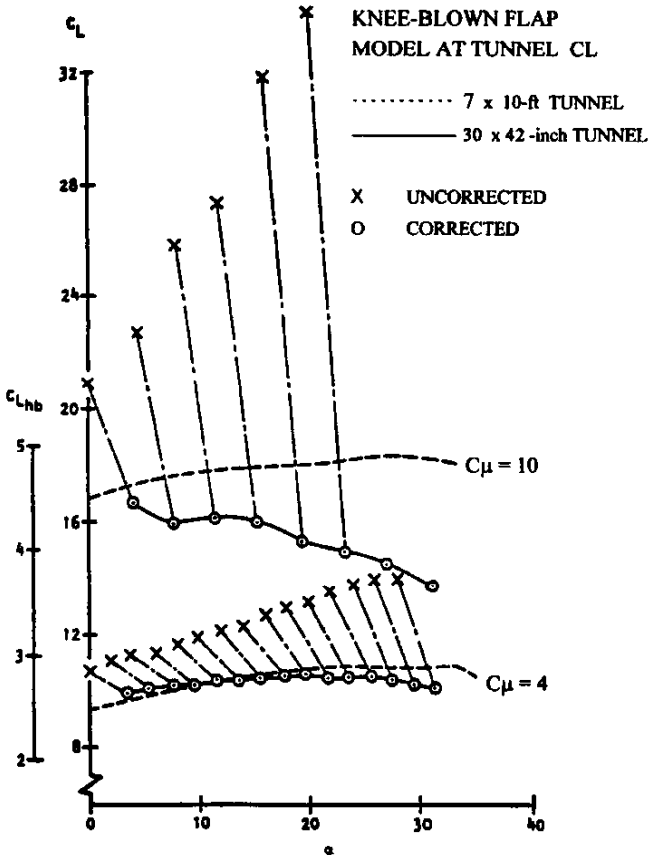


Figure 8.7 Constraint Corrections under Very High Blockage Conditions

### 8.1.2.6 TUNNEL INDUCED GRADIENTS.

The presence of very large interference effects implies correspondingly large tunnel-induced gradients. These are of concern, particularly with regard to control surfaces. The topic will be revisited as part of the discussion of correction procedures in the following sections.

### 8.1.2.7 'STIFFNESS' OF POWERED FLOWS.

An obvious concern when tunnel interference is large, or when a powered flow intersects a surface, is that the powered wake will distort. This is clearly the case when a jet or rotor wake hits the floor and some correction procedures recognise this by providing a theoretical extension as part of the correction process. However, the question remains whether the wake is distorted nearer to the model. This issue was investigated by Hackett et al [16] who showed that, for round jets at least, the jet trajectory is

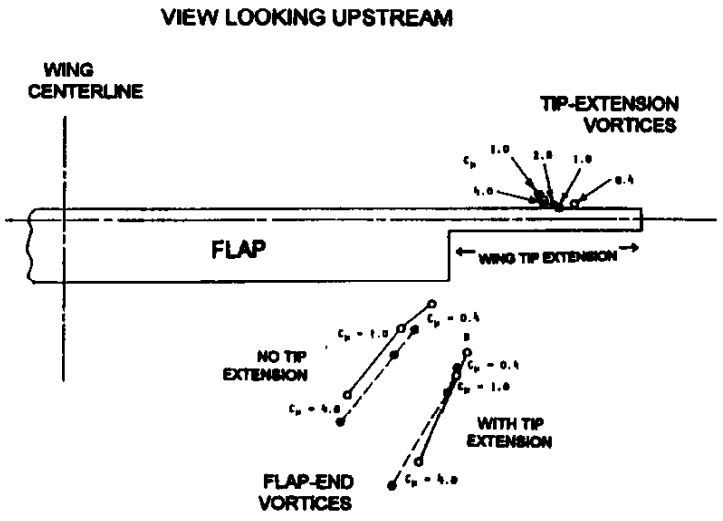


MODEL DETAILS
Wing Sweep = 25 deg
Nominal Chord = 5,13" (constant)
Aspect Ratio = 6.0 (no tips)
Aspect Ratio = 9.0 (with tips)

TUNNEL DETAILS
Traverse X/C = 5.13
Filled Points : 10 x 7-ft tunnel
Open points : 43 x 30 inch tunnel

Figure 8.8 Measured Vortex Positions Behind a Knee-Blown Flap Model at Various Power Settings, in Small and Large Wind Tunnels

changed only within one or two jet diameters of the impact point. This is reassuring for jet-powered configurations but it remains of concern for rotor testing.

Figure 8.8, taken from Hackett et al [7], shows small and large tunnel trailing vortex positions for a swept-wing version of the knee-blown flap model mentioned previously. The vortex positions were determined using a rotating vorticity meter. The model was tested at several flap blowing levels with and without wing tips. Neither flap blowing level nor tunnel size had much effect on the positions of the vortices springing from the extended tips, when these were fitted. However, the flap-end vortices penetrated the flow increasingly as blowing level was increased, whether or not the extended tips were present. As might be anticipated, the flap-end vortices penetrated more deeply into the large tunnel flow as corrected $C_\mu$ was increased. On rotating the co-ordinate system by the tunnel-induced angle-of -attack, however, it was found that the vortex positions were essentially the same for both large and small tunnels. Wake yielding due to tunnel-imposed velocities was thus found to be insignificant for this configuration, provided flow rather than tunnel axes were used.

### 8.1.2.8 OTHER CONFIGURATIONS

A specific, blown-flap configuration has been used in the example above to illustrate some of the principles involved in powered lift testing. The range of possible V/STOL configurations is too large for individual treatment to be practical here. Multiple jet, multiple fan or multiple rotor configurations present special difficulties in this regard. Specialised instrumentation, data handling and constraint corrections may be needed in these cases. However, it can probably be assumed that the flow physics of each power unit will be similar to a unit acting alone and a similar approach can be applied. Closely spaced units should probably be treated as one.

## 8.2 FLOW MODELLING-BASED METHODS.

### 8.2.1 HEYSON'S METHOD

#### 8.2.1.1 INTRODUCTION

One of the earliest schemes for modelling V/STOL flows is given in Heyson [22]. His tunnel correction method was developed originally for single-rotor helicopters and was extended over a period of several years to include additional V/STOL configurations, several of which were checked out in the wind tunnel. The extensive collection of literature concerning Heyson's methods includes NACA and NASA reports, tech notes, memos and special publications, many of which are employed in this chapter as definitive references (see Heyson [22] through Heyson [34]). The mathematical developments and code listings are voluminous and no attempt will be made to reproduce them here. Rather, we shall try to highlight the physics and methods involved in Heyson's method, point out known limitations and errors and make appropriate references to the source material. Examples of its application to selected V/STOL examples will be included. Other reviews may be found in Rae and Pope [37] and in a review report by Olcott [36], which is more comprehensive.

It is important to note, at the outset, that Heyson's method models only the non-viscous flow. Drag input to the method, for example, thus includes only induced drag, which may be difficult to estimate for many powered flows. Blockage due to viscous drag must be estimated separately.

#### 8.2.1.2 HELICOPTER ROTORS

The flow beneath a helicopter rotor in still air can be represented by a vortex tube built of vortex rings that lie parallel to the rotor disc. Vortex ring strength is defined by rotor lift and slipstream contraction is neglected. As the helicopter moves forward, or the tunnel is turned on, the vortex cylinder is sheared in the downstream direction and the intersection with the ground or the tunnel floor moves aft. If free-air results are the objective, there is a minimum forward speed below which flow reversal along the tunnel floor invalidates the data. If in-ground effects are required, the situation is more complicated because some forward flow is possible in flight cases (see Section 8.1).

In the theoretical development of Heyson [22], each vortex ring is first replaced by a circular sheet of doublets. The sheet is then condensed to a point. The original sheared vortex cylinder becomes an inclined line of doublets extending from the rotor centre to

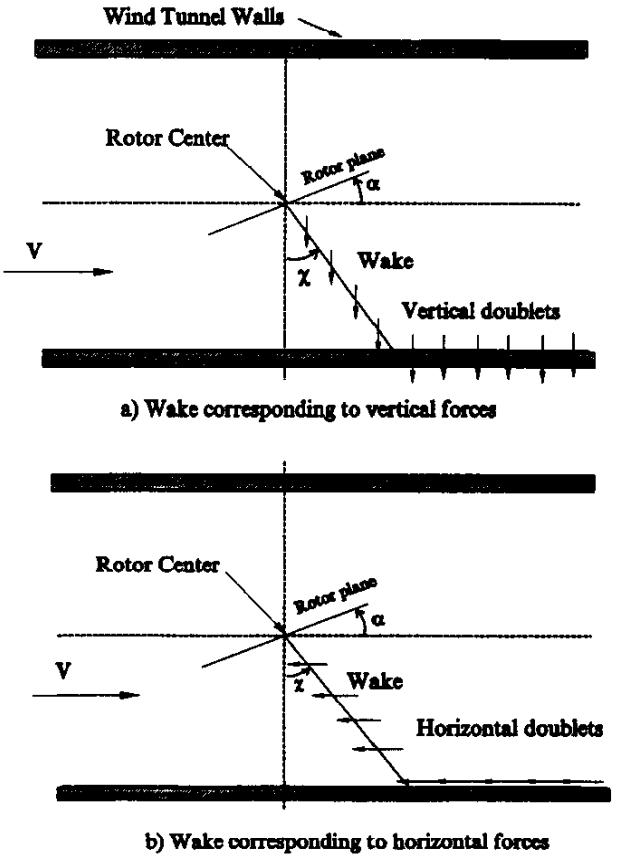


Figure 8.9 Rotor wake model used by Heyson

the floor as illustrated in Figure 8.9(a). The wake deflection angle is determined primarily by the lift-to-drag ratio for the particular data point concerned; the full analysis will be described below. Figure 8.9(b) shows horizontal doublets that also populate the wake. These were introduced to accommodate cases for which the jet axis is inclined at angle $\chi$ to the vertical. The vertical and horizontal doublet strengths are *proportional to cosine $\chi$ and sine $\chi$ respectively*.

On reaching the tunnel floor, the doublet line trails downstream. Each vertical doublet is cancelled by its image in the ground or tunnel floor, but the horizontal doublet vectors are additive. Tunnel effects due to the images of the system in Figure 8.9 are calculated using classical imaging techniques. Heyson's *method reconstructs the "missing" part of the jet plume that has been cut off by the tunnel floor. (see also "Generation of interference coefficients"* later in this chapter). A similar procedure is employed when applying the wall pressure signature treatment to jet-plumes, described in Section 8.3.

Tunnel interference for a finite wing can be determined as a special case of the system just described in which the line of vertical doublets trails aft and never intersects the floor. Because of differing definitions, there is a factor of minus four between Heyson's boundary correction factor and the classical value (see page 12 of Heyson [22]. Table 5 of the same reference demonstrates close agreement between Heyson's formulation and the classical values for wings in closed and in three-quarters-open wind tunnels.

### 8.2.1.3 DUCTED FLOW

*The flow within a jet emerging from a duct at right angles to a mainstream can be thought of as being* generated by a doubly infinite vortex tube with strength equal to the velocity jump across the jet boundary. The vorticity tube comprises boundary layer fluid on the duct walls, then a cylindrical shear layer when the fluid leaves the duct. A point at the centre of the jet exit plane 'sees' the full jet velocity because the vorticity tube is doubly-infinite. The Heyson model is *semi*-infinite, however, because the vorticity is generated at the rotor tips and does not extend above the rotor plane. Consequently, the velocity at the rotor centre is only half of that for the doubly-infinite system. For this reason the original interference factors must be multiplied by a factor of two ('n', in equations 8.3 to 8.5, below) for jet-powered cases (see also Appendix A of Heyson [31]. Options are provided in the Heyson algorithm for *rotors, wings and jets*.

An idealised V/STOL lifting jet or a control jet emergent from an aircraft surface may include a long approach region upstream of its exit plane. The doubly-infinite doublet line is usually a reasonable far-field approximation in such cases. However, the duct length ahead of the exit plane for realistic V/STOL configurations is finite and a factor of two will overpredict the interference. Engineering judgement is required to terminate the doublet line appropriately at its upstream end. Further details concerning the relationships between the corrections for rotors, wings and jets may be found in Heyson [31], Appendix A.

### 8.2.1.4 EXAMPLES OF ROTOR INTERFERENCE FLOW FIELDS, ACCORDING TO HEYSON

Figure 8.10 shows interference fields in a square tunnel, taken from Heyson [31]. The rotor spans 60% of the tunnel width and is positioned 15% of the tunnel height above the centreplane. The upper two plots *depict upwash and axial interference velocity for a skew angle of 10-degrees, a near-hover condition.* A downwash interference of approximately 1.0 is observed near to the tunnel floor (upper plot) where the rotor wake impacts the floor. The u- component interference is near zero at this point (second plot from

top). At higher forward speed (lower two plots), the impact region moves downstream and a streamwise downwash gradient appears in the plane of the rotor. At both forward speeds the u-component interference in the wake region is much greater than that in the rotor plane.

### 8.2.1.5 LARGE ROTORS

In cases for which the small-rotor assumption is invalid, Heyson uses multiple doublet lines, distributed through the rotor wake cylinder as shown in Figure 8.11. The enclosing cylinder in the sketch is the true vorticity cylinder. Heyson (1970) points out that there are difficulties associated with 'lumpiness' that affect both the rotor plane and the floor impact region. As he explains, these difficulties are also present in Heyson (1969 a) and Heyson (1969 b).

Even at low forward speed the assumption of uniform disc loading may be in question for large rotor diameters because the blade tips are highly loaded. The representation of triangular blade loading, using concentric vortex cylinders, is discussed in Appendix B of Heyson [31], and in Heyson [21].

At intermediate forward speeds, the load distributions on advancing and retreating rotor blades may differ significantly even though the total lift is centred (zero rolling moment). This further invalidates the assumption of uniform disc loading. Under these conditions the correct interference flow field for a large rotor would be expected to be asymmetric about the tunnel centre plane. No method appears to be available that deals with this situation. In counterpoint, it should be noted that a helicopter wake at high forward speed becomes very wing-like at an advance ratio of 0.095, for example (See Figure 46 of Heyson [21] or Figure 8 of Heyson [32]). It is also found that tunnel corrections for a finite wing of aspect ratio $4/\pi$ (i.e. the aspect ratio of a disc) work well when applied to a helicopter rotor at high values of advance ratio (see Heyson et al [21]).

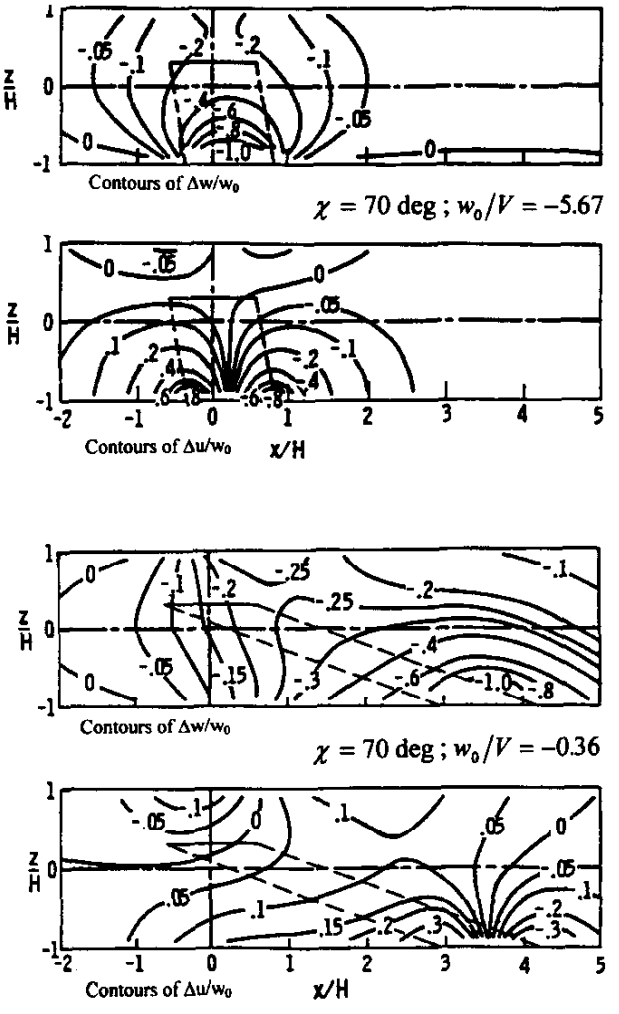


Figure 8.10 Wall induced interference velocities for a uniform loaded rotor mounted 30% of a semiheight above the centreline of a square, closed wind tunnel. σ = 0.6

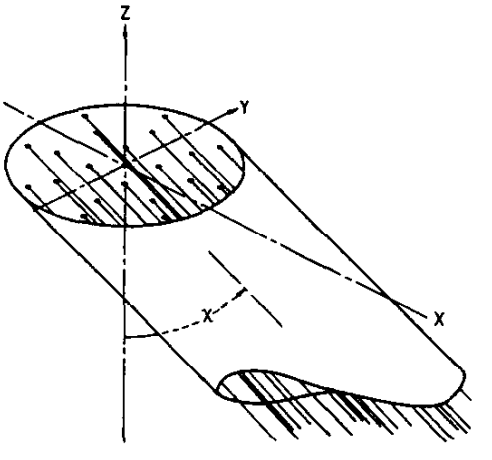


Figure 8.11 Sketch of a skewed cylinder of vorticity and the doublet-line system used to represent it.

### 8.2.1.6 DETERMINATION OF WAKE SKEW ANGLE, $\chi$

The wake skew angle, ($\chi$ in Figure 8.9), is a major parameter in determining the tunnel corrections for powered lift models when using Heyson's method. To some approximation, it represents the trajectory of the wake. The measurement of $\chi$ from the vertical reflects its helicopter origins. However $\theta$, the complement of $\chi$, defines the deflection of the wake from the horizontal.

As originally defined for rotors (e.g. Heyson [24]) $\chi$ was based strictly on momentum theory (see below). The wake was assumed to be infinitely stiff and its initial slope at the rotor plane was assumed to persist until the wake impinged upon the tunnel floor. In Heyson et al [26], and subsequently, the fact was recognised that wake penetration is reduced by the action of the mainstream. To accommodate this, the momentum-based deflection angle, $\theta$, was reduced to ½ $\theta$. This is equivalent to replacing $\chi$ by an effective value $\chi_e$ = ½ ($\chi$ + 90) deg. This is implausible near to hover because $\chi_e$ becomes 45-degrees. However, Heyson et al [27] argue that "there are limitations on the minimum speed at which tests can be made in a meaningful fashion in wind tunnels, and it is believed that these limitations will generally be encountered before the failure of (the above approximation)". Recognising the difficulty, Heyson [30] states that "Even though experimental studies indicate remarkably improved agreement between comparative tests when the above relations are used, it is obvious that there is a limit to their applicability". Figure 3 of the same reference suggests other, more plausible definitions. However, most of Heyson's results use the ½ $\theta$ assumption.

It is important to note that the $\chi$ value determined from Equations 8.1 through 8.8, below, *is* momentum-based. $\chi_e$ represents only the vortical part of the wake and applies only to the tunnel interference part of the calculation. There is some justification for this in the flow physics since the trailing vorticity peels away from the sides of the powered jet, which then tends to maintain its original direction. Only far downstream (if ever) does the jet fluid become fully entrained into the vortex system. The half-angle assumption is also consistent with the situation in the wake of a finite wing, for example, for which the deflection of the trailing vortices from the horizontal is half of that for the central wake. The symbol $\chi_e$ is not used by Heyson but is introduced here, and also in Rae et al [37], for clarity.

### 8.2.1.7 EFFECTS OF REPLACING $\chi$ BY $\chi_E$

One of the main motivations for revising the definition of skew angle concerned pitching moments. In a particular fan-in-wing study (Heyson et al [27]) tunnel corrections based on $\chi$ were of approximately the right magnitude, but of the wrong sign. It is apparent from Figure 8.12 (a) that the use of $\chi_e$ , rather than $\chi$ , shifted the peak downwash due to lift from a wing location to the tailplane. Figure 8.12 (b) shows that $\chi$ -based pitching moment corrections had the wrong sign, whereas $\chi_e$ -based corrections (Figure 8.12 (c)) worked well. It is understood (Margason [35]) that these benefits were obtained without seriously compromising the lift and drag correlations.

### 8.2.1.8 GENERATION OF INTERFERENCE COEFFICIENTS

Having established the theoretical jet trajectory, now at angle $\chi_e$ to the vertical rather than $\chi$ as in Figure 8.9, and knowing that the doublet vector is aligned with it, the tunnel interference may be calculated. This is achieved by determining the effects of a classical, doubly-infinite set of images in the tunnel walls. The basic formulation is given in Heyson [22] as Equations 18 and 19. The inclined line doublet and its image

in the tunnel floor are considered as a unit that comprises four inclined semi-infinite doublet lines. Line 1 extends from the model centre at angle $\chi_e$ and continues downward through the tunnel floor to infinity. Line 2, which is applied negatively, overlays the lower part of Line 1 and cancels the part below the floor. Lines 1 and 2 therefore describe just the (inclined) in-tunnel line doublet. Lines 3 and 4 are used similarly to create the corresponding finite length ground image doublet. This completes the central tunnel-plus-ground-image unit.

The effects of the entire image set, excluding the central unit, are double-summed in the usual way to determine the tunnel interference. Since the basic unit includes the ground image, this means that, in leaving out the central unit, the ground image is excluded as well as the in-tunnel line doublet. The summation over the tunnel image set therefore gives the tunnel correction for the ground effect case. To obtain the tunnel correction for the free air case, the effects of Lines 2, 3 and 4 are added back, with due regard for their sense. These are the three trailing terms in Equation 19b of Heyson [22]. Additional details may be found on page 13 of Heyson [25].

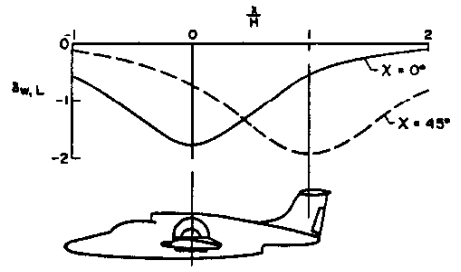


(a) Effect on downwash distribution

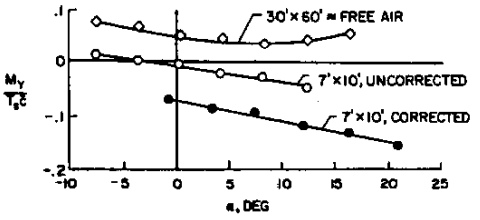


(b) Pitching moment correlation for original definition of $\chi$

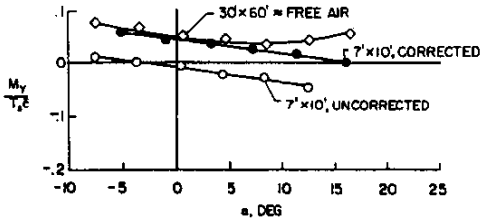


(c) Pitching moment correlation for revised definition of $\chi$

Figure 8.12 Changes in downwash distribution and pitching moment due to redefined wake skew angle.

The interpretation of the added-back terms, Lines 2, 3 and 4, is important. As already indicated, Lines 3 and 4 are conventional images that represent the ground image of the in-tunnel wake. However, Line 2 is *not* the image of anything but is, rather, the below-floor extension of the inclined, in-tunnel line doublet downward to infinity. Its effect is subtracted from the value of $\delta$ which is, itself, a subtracted quantity. Line 2 therefore *adds* the effects of the wake extension to the solution. This means that the Heyson solution adds back the effects of the wake extension below the tunnel floor that would have been present in free air: it reconstructs the 'missing' part of the wake as well as providing image effects.

### 8.2.1.9 APPLICATION OF INTERFERENCE COEFFICIENTS.

The interference factors, $\delta_{w,L}$, $\delta_{u,L}$, are used to determine tunnel-induced vertical and horizontal velocity associated with lift. $\delta_{w,D}$ and $\delta_{u,D}$ are the corresponding factors associated with drag. They are plotted typically as a function of $\chi$, the momentum-based skew angle, with tunnel width-to-height ratio, $\sigma$, as a parameter. Numerous plots of this type may be found in Heyson [25], for example. Figure 8.13, adapted from Heyson [23], shows the variation of the four interference factors with x/H for various skew angles.

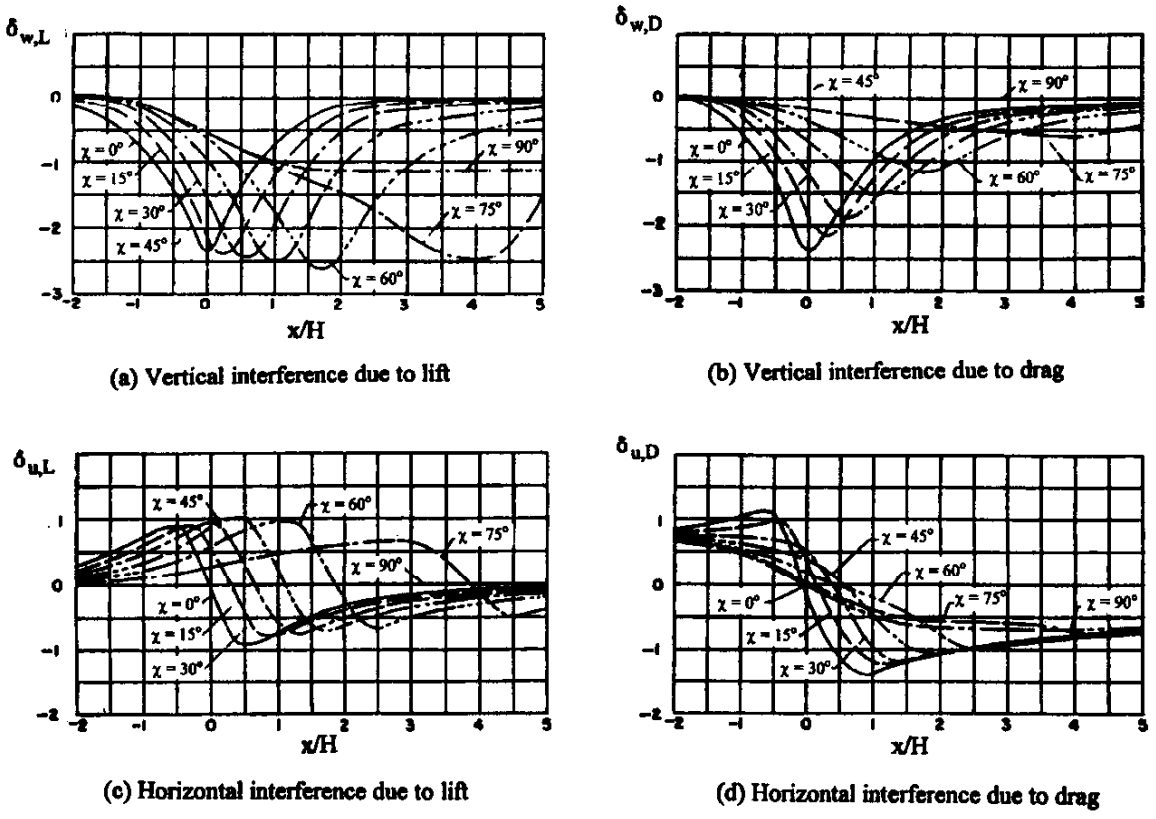


(a) Vertical interference due to lift

(b) Vertical interference due to drag

(c) Horizontal interference due to lift

(d) Horizontal interference due to drag

Figure 8.13 Examples of Interference coefficients

$\delta_{w,L}$, $\delta_{u,L}$, $\delta_{w,D}$ and $\delta_{u,D}$, are normalised on $u_0$ or $w_0$. The parameter $w_0$ is defined in Heyson [24] as "the vertical induced velocity, at the force-generating system, required to produce a given vertical force, positive upward". $u_0$ is defined similarly for horizontal force. For a helicopter, "at the force generating system" means at the rotor hub. The wake skew angle (Figure 8.9) is then given by

$$\tan \chi = \frac{V + u_0}{-w_0} \tag{8.1}$$

where V is the mainstream velocity. The resultant velocity $V_R$ is given by

$$V_R = \sqrt{(V + u_0)^2 + (-w_0)^2} \tag{8.2}$$

If the characteristic velocities in the far wake are $nw_0$ and $nu_0$ the lift and induced drag are given by

$$L = \rho A_m V_R (-nw_0) \tag{8.3}$$

$$D_i = \rho A_m V_R (-nu_0) \tag{8.4}$$

Now define a reference velocity $w_h$ as the value of $w_0$ that would be required to hover with zero speed and induced drag and the same values of n and $A_M$ that pertain to forward flight (see Heyson [31] for a more comprehensive development). Thus:

$$w_h = -\sqrt{\frac{L_h}{n\rho A_m}} \qquad (8.5)$$

where the negative sign is required because positive lift requires negative induced velocity. The value of n is 2 for a rotor or wing and 1 for a ducted jet. $A_m$ is the momentum area of the aerodynamic force generating system; the rotor disc area for a helicopter or the exit area for a jet. The momentum area for a wing is ($\pi$/4) times span-squared. The parameter n expresses the change in effective velocity $w_0$ between the rotor plane, for example, and a location far downstream where slipstream contraction is complete.

Substituting equations 8.3 and 8.4 into 8.2 and normalising on $w_h$ yields, (see Heyson [24]):

$$\left(\frac{w_0}{w_h}\right)^4 = -\sqrt{\frac{1}{1+\left(\frac{V}{w_0}+\frac{D_i}{L}\right)^2}} \qquad (8.6)$$

In equation 8.6, V is the mainstream velocity, $D_i$ is estimated from measured drag, L is measured lift and $w_h$ is determined from equation 8.5. Equation 8.6 is implicit in $w_0$. Figure 2 of Heyson [24] is a nomographic procedure used to determine $V/w_h$ (see also Figure 6 of Heyson [25]). $(V/w_0)$ is then determined using $(V/w_0) = (V/w_h)/(w_0/w_h)$. One more chart look-up is then performed to determine $\chi$, which is a unique function of $(w_0/w_h)$. There is now sufficient information to construct the flow model and determine the four interference $\delta$'s. The subsequent procedure is described in Appendix C of Heyson [25], which details the entire twenty-eight step process.

### 8.2.1.10 ALTERNATIVE INTERPRETATION OF THE SOLUTION PROCESS

Equation 8.6 may be expanded to give

$$\left(1+\left(\frac{D_i}{L}\right)^2\right)\left(\frac{w_0}{w_h}\right)^8 + 2\left(\frac{V}{w_h}\right)\left(\frac{D_i}{L}\right)\left(\frac{w_0}{w_h}\right)^7 + \left(\frac{V}{w_h}\right)^2\left(\frac{w_0}{w_h}\right)^6 - 1 = 0 \qquad (8.7)$$

Equation 8.7 is an octic in $(w_0/w_h)$ in which all of the coefficients and $w_h$ are known. In effect, the nomographic approach of Heyson [24] solves this equation and selects the appropriate root.

We obtain $u_0$ using the auxiliary equation

$$u_0 = w_0\left(\frac{D_i}{L}\right) \qquad (8.8)$$

which is obtained by dividing equation 8.3 by equation 8.4.

Finally, we substitute $u_0$ and $w_0$ into equation 8.1 to obtain $\chi$. Construction of the in-tunnel flow model is completed by converting the momentum-based value of $\chi$ to the effective value, $\chi_e$, as described previously.

Chart look-up or equivalent computer code is used to determine $\delta_{w,L}$, $\delta_{u,L}$, $\delta_{w,D}$ and $\delta_{u,D}$. These interference coefficients are then re-normalised on mainstream velocity using:

$$\frac{\Delta w_L}{V} = \delta_{w,L}\left(\frac{A_m \rho_0 w_0}{A_T \rho V}\right)$$

$$\frac{\Delta u_L}{V} = \delta_{u,L}\left(\frac{A_m \rho_0 w_0}{A_T \rho V}\right) \qquad (8.9)$$

$$\frac{\Delta w_D}{V} = \delta_{w,D}\left(\frac{A_m \rho_0 u_0}{A_T \rho V}\right)$$

$$\frac{\Delta u_D}{V} = \delta_{u,D}\left(\frac{A_m \rho_0 u_0}{A_T \rho V}\right)$$

where $A_T$ is the tunnel cross sectional area, $\rho_0$ is the density of the powered flow and the remaining symbols are as defined previously.

### 8.2.1.11 SAMPLE RESULTS FOR V/STOL CONFIGURATIONS

Heyson [25], [26] and [33] give examples of the application of his correction procedures to V/STOL configurations. A summary is given in Heyson [32]. Somewhat surprisingly, in view of the method's origins and current use, it is difficult to find a good example for a pure helicopter. This is partly due to the fact that reliable small/large-tunnel helicopter test comparisons are very difficult to do but also because Mr Heyson's assignments within NASA were out of phase with the helicopter testing of that time (see Margason [35]).

Limited V/STOL examples will be given here that compare corrected data from models in a 7- by 10-foot test section with results measured in a 17-ft test section. All the present examples were taken from Heyson [25], which includes ground-effect cases and other V/STOL configurations.

Figure 8.14(a) shows lift and drag data for a 3.36-ft semi-span jet-flapped model prior to applying corrections. The flap angle was 60-degrees. A significant difference in stall angle may be seen. On applying first-level corrections (not shown), the stall angle difference was largely resolved, but a significant $C_L$ discrepancy of about 1.0 arose, the small tunnel value being greater. This was consistent with the fact that corrected $C_\mu$ values differed by 0.62. Figure 8.14(b) shows good correlations after correcting the results to a common $C_\mu$ value of 6.75.

Figures 8.15(a) and (b) show data for a tilt-wing VTOL configuration before and after correction. In this case correction to a common $C_T$ was not possible. Heyson [25] points out that the corrections are significant even for the large tunnel in this example. The fact that corrections to drag in the small tunnel move the upper part of the polar from drag to a thrusting condition has obvious performance implications.

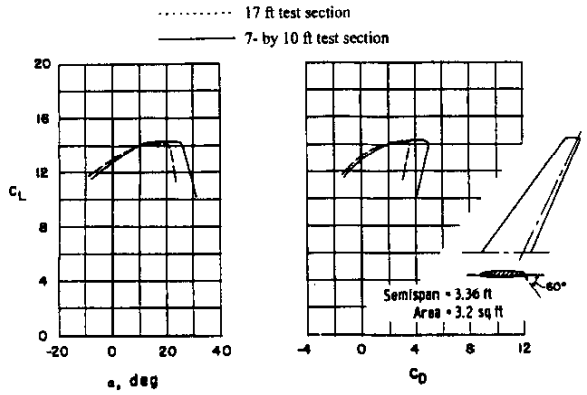


(a) As tested at Cμ = 6.20 with no tunnel corrections

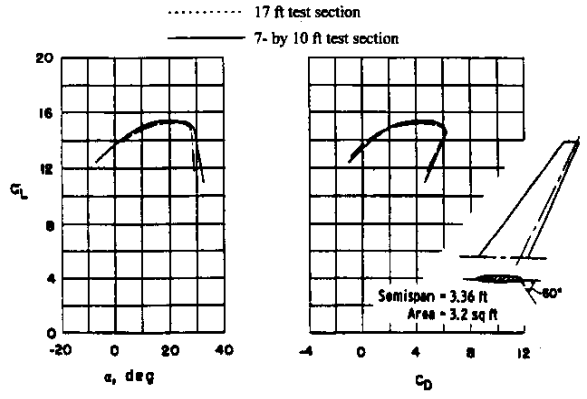


(b) With tunnel corrections and additional corrections to Cμ = 6.75

Figure 8.14 Application of Heyson's corrections to a swept-wing jet flapped model at very high lift

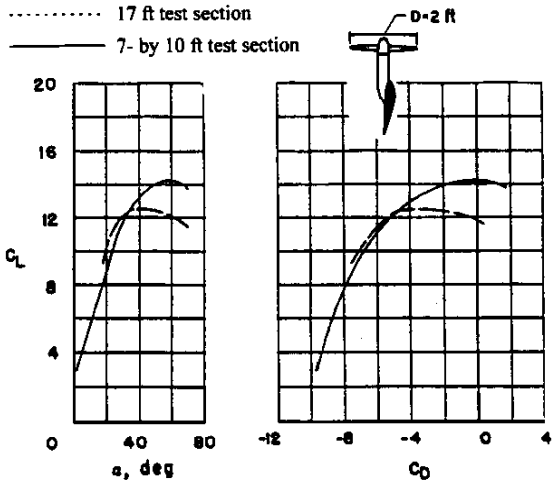


(a) As tested at CT = 10.3 with no tunnel corrections

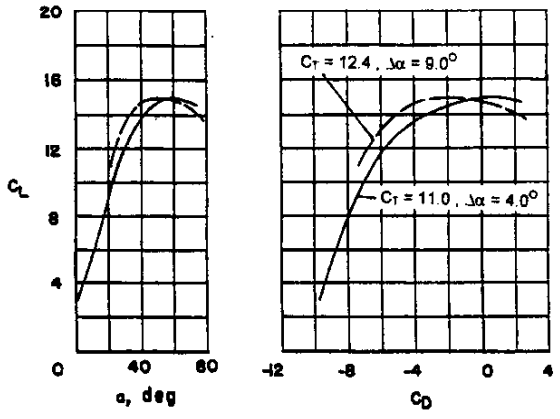


(b) With tunnel corrections

Figure 8.15 Application of Heyson's Correction to a tilt-wing VTOL configuration

The ducted fan, in the example of Figure 8.16, has an area of only 2% of the 7- by 10-foot tunnel area but nonetheless the correction is noticeable (Figure 8.16(b)). In this case the $C_T$ discrepancy is only a few percent and the curves correlate quite well without further adjustment.

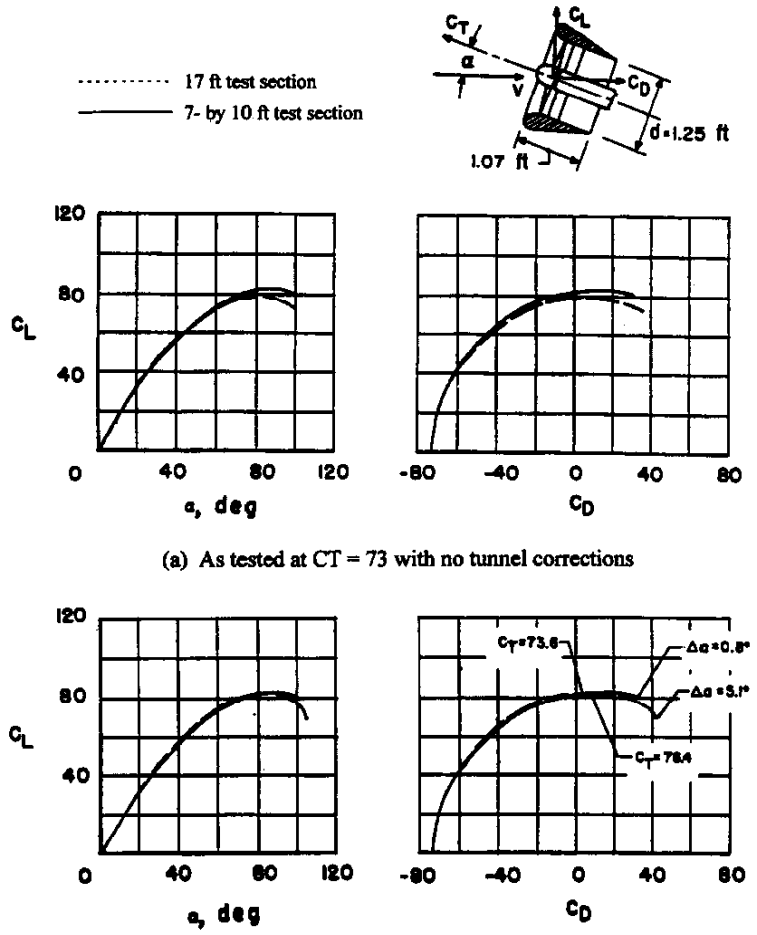


(a) As tested at CT = 73 with no tunnel corrections

(b) With tunnel corrections

Figure 8.16 Application of Heyson's correction to a ducted fan configuration

## 8.2.2 PANEL METHODS.

Panel methods may be thought of as a bridge between the classical potential flow methods and more recent approaches based on wall pressure measurements (see Section 8.3). They permit larger model size and give more geometric flexibility; considerable detail is possible. However they do not automatically accommodate viscous effects or power effects which, if used, have to be added explicitly. The discussion in this section will be limited to the special needs of V/STOL flow representation. A more general description of panel methods may be found in chapter 2.3.

A principle difficulty in modelling V/STOL powered flows concerns the fact that the jet trajectory and cross sectional shape are usually unknown and cannot be measured readily. This was circumvented in the Heyson approach, above, by assuming a straight-line jet trajectory at an empirically determined angle. Other approaches employ more sophisticated empirical shapes based on experimental trajectories, as in Section 8.4, for example. The jet cross sectional shape is usually of secondary importance for far field calculations, such as wind tunnel effects, provided that the local turning forces are represented.

A second difficulty concerns the representation of bi-energy flows. We saw in Section 8.2.1 that a vortex ring cylinder, or its equivalent, is needed to represent a large helicopter wake properly. In the examples quoted in the previous section, Heyson shrinks the ring cylinder to a line, thereby preserving the thrust but eliminating the high energy part of the real flow. If a semi-infinite, constant-strength vortex tube is employed, an actuator disc is implied at the rotor plane that provides a uniformly distributed jump in velocity potential (total pressure). Strictly, the wake of an open rotor should be relaxed to allow slipstream contraction to occur, as for propellers (see previous chapter), but this is not usually done in tunnel effects applications. In a ducted flow, a semi-infinite vortex ring cylinder may be placed in the duct, to provide the energy jump, and radial equilibrium may be achieved by specifying a Neumann boundary condition (zero normal flow) at the duct wall.

Panel methods can be used to address both of the above difficulties. An early example (Figure 8.17) concerns the Boeing fan-in-wing program (See Rubbert et al [38]). This application was designed for free air performance estimation. However with the computing power now available, the method could also be used for estimating tunnel effects, by adding panelled tunnel walls, for example. In Figure 8.17, a panelled cylinder is wrapped around an empirically determined plume trajectory. Doublet panels were employed and the Neumann boundary condition was imposed at the centre of each. The boundary condition is specified all the way around the periphery of the cylinder so the effects of the exterior flow around the jet body are included.

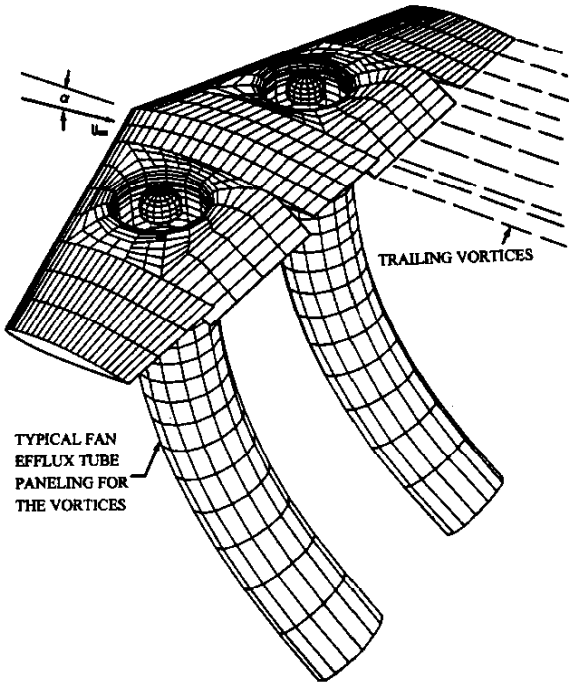


Figure 8.17 Application of a panel method to a fan-in-wing configuration

The fan face is also represented by doublet panels but a finite, rather than a zero normal velocity is imposed there. No attempt is made to simulate the fan's geometry or its pressure rise characteristic. Directly specifying the velocity through the fan defines the jump in potential (and total pressure) across it. Since, at forward speed, there would be a finite velocity through the fan plane in free flow (i.e with the fan-face boundary condition unspecified), the actual jump in potential is determined by the difference between this free flow and the imposed velocity. This makes it very difficult to estimate the boundary condition that would provide a constant total pressure rise across the fan, for example. A poor choice of imposed velocity could even lead to pressure *loss* through the fan plane. Assumptions concerning this boundary condition therefore need to be made with considerable care and the use of experimental measurements at the fan inlet may be appropriate. Rubbert [38] shows significant flow changes as the imposed inlet velocity distribution is changed.

Viscous effects are simulated in Rubbert [38] using simplified strip methods: the same approach could be applied to the wind tunnel walls, including the effects of model-imposed pressures. While this might account for most of the viscous effects, wall pressure based methods are needed to capture the full interaction.

## 8.3 THE WALL PRESSURE SIGNATURE METHOD

### 8.3.1 THEORETICAL OVERVIEW

The pressure signature method uses pressure measurements ("signatures") along the tunnel wall, roof and floor centreline to determine the tunnel interference at locations on the test model. The pressure data, interpreted as streamwise velocities, are used to determine the strengths and locations of line sources and horseshoe vortices that constitute a simplified theoretical model of the object being tested. The underlying theory is developed in Section 4.1.3. This contrasts with the two-variable method (Section 4.1.4), which requires full area coverage of all four tunnel surfaces but requires no representation of the model. The pressure signature method has been employed for powered flows for about twenty years. There is much less powered flow experience with the two-variable method (see Ashill and Keating [1]).

The discussion that follows deals with practical aspects of applying the pressure signature method in its various forms. The underlying mathematical development is given in Section 4.1.

#### 8.3.1.1 THE THREE DIMENSIONAL INVERSE PROBLEM.

The first task when using the pressure signature approach is to determine a theoretical flow model of the object under test in the wind tunnel using limited geometric information. This flow model includes a classical set of wall images. The output from the first task comprises the strengths and locations of the model elements; sources, sinks and horseshoe vortices. With these established, the second task - finding the interference at the model - is straightforward. This is accomplished by calculating the velocities induced at the model location by the tunnel image system. The effects of the tunnel-induced flow on model forces and pressures can then be determined.

The crux of any pressure signature method lies in determining the theoretical model. This particular three dimensional inverse problem is unusual because the boundary condition is specified at locations that are remote from the generating elements. The element locations are unknown and the expressions for induced velocity at the walls, due to model elements, are non-linear in X, Y and Z, the space co-ordinates. The problem to be solved is therefore algebraically non-linear. The fact that the theoretical model includes an infinite array of tunnel-surface images leads to very complicated equations with little prospect for a closed-form solution (see Hackett et al [12]), Appendix IV). Several different solution methods have been employed.

#### 8.3.1.2 NON-LINEAR SOLUTIONS

Figure 8.18 (upper) shows the original theoretical flow model used for blockage solutions by Hackett et al [8] and subsequently (e.g. Hackett et al [12]). The lower plot shows how the solid and wake blockage contributions combine to give the total tunnel wall signature. The theoretical model comprises a solid-blockage line source and line sink, total strengths $+Q_s$ and $-Q_s$ , located on the tunnel centreline at $X_3$ and $X_4$ (Figure 8.18), and a wake line source, total strength $Q_w$ , at station $X_2$ . The solid blockage source-sink spans $b_3$ and $b_4$ are equal but different from $b_2$. There are thus three unknown locations, two unknown spans and two unknown strengths, for a total of seven variables. The five geometric variables are non-linear; the two strengths are linear. Hackett et al [8] found non-linear solutions for a 9.53% normal flat plate using seven points selected from a measured wall signature. Multiple solutions are possible because the problem is non-linear: the particular root obtained depends upon the initial estimate given to the solver. Complex-number solutions have no meaning in the present context and can be

discarded. Three non-linear solutions were compared with results obtained using the chart look-up approach that eventually became standard for many applications (see Section 8.3.3). This showed that all of the calculated interference distributions lay within a narrow band, even though the geometry and element strengths varied significantly among the several solutions.

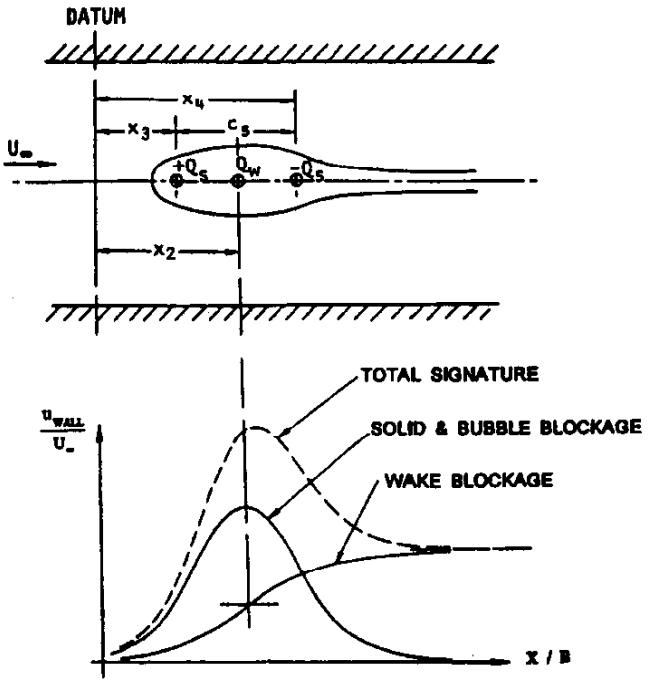


Figure 8.18 Flow model for the "Source-Source-Sink" version of the pressure signature method

The full non-linear, seven variable approach is impractical for real-time use so additional assumptions were made to make the logistics more manageable. The source spans, which were found to be weak variables, are now estimated from the model geometry and it is assumed that all the spans are equal and that the wake source is positioned midway between the solid blockage source and sink. This approach, which has become known as the "source-source-sink method", leaves four quantities to be determined, $Q_w$, $Q_s$, $X_2$ and $c_s$ (see Figure 8.18). The problem remains non-linear, however, and iteration is needed to find the solution. Results using this approach fall within the same band as for the seven-variable approach just described. (See Hackett et al [8]). Section 8.3.3 will describe the production implementation of the "source-source-sink" approach. Conventional angle of attack corrections are used in conjunction with this version.

It is possible in principle to consider an analogous non-linear approach for tunnel-induced upwash, using horseshoe vortices instead of line sources. However, in the context of the high lift situations for which the method was developed, interactions between lifting and blockage flows might make it necessary to couple the two solutions. For example, vortex-generated upwash, at the sidewalls, can be sufficient at very high lift to affect the sidewall blockage signatures. It was therefore decided to adopt a linear approach for combined lift and blockage interference (see below and Section 8.3.4)

### 8.3.1.3 Linear Solutions

During the early development of the pressure signature method, there was interest in applying it on-line so as to test at "true-q". Though the source-source-sink approach is reasonably efficient, the computers of the day were marginal for this task and a faster code was required. This provided additional incentive to develop the "matrix" version of the pressure signature method.

Fixed-span, fixed-location elements are used under the matrix method, thereby removing the non-linear geometric variables from the problem and leaving only element strengths as unknowns. An influence matrix is calculated for the measurement locations at the tunnel walls, including the effects of the full tunnel image system, as before. Typically, a source array might now include ten elements of unknown strength distributed uniformly from the model nose to a location in the wake.

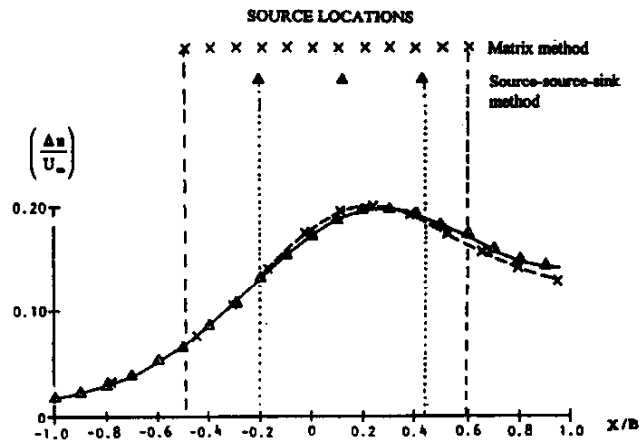


Figure 8.19 Centreline blockage distribution for a 9.53 % normal flat plate

In a practical installation, designed to accommodate a variety of models and test conditions, the number of wall pressure measurements may be several times the number of elements used in the theoretical model, so a least-squares solution is required. Figure 8.19, which uses the same 9.53% normal plate pressure signature as the example quoted above, shows results for the source-source-sink and matrix solutions as triangles and crosses respectively. It is apparent that the solutions are very similar, despite the fact that the element distributions differ significantly.

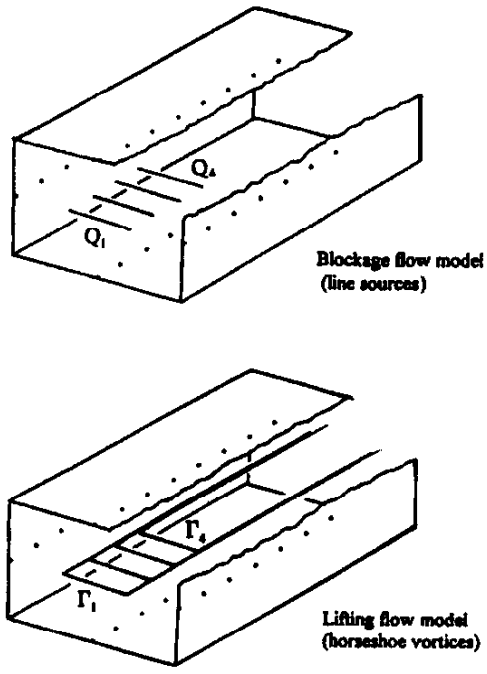


Figure 8.20 Flow model for the "Matrix" version of the pressure signature method

Influence coefficients for horseshoe elements add further columns to the influence matrix, which is solved using least-squares as before. Figure 8.20 shows the arrangement of four line sources and four horseshoe vortices in the wind tunnel. More elements than this are usually employed. Section 8.3.4 describes the implementation of the matrix method. A description is included of how the blockage/lift interaction, mentioned above, is handled.

### 8.3.1.4 QUASI-LINEAR SOLUTIONS

Hackett et al [14] and, more recently, Rueger, Crites et al [39] mention the proclivity of the matrix version of the pressure signature method to produce oscillating-strength solutions. In neither of the instances quoted was this harmful to the resulting interference distribution. These examples reflect the ill- conditioning that is common in influence matrices of the present type (see also Section 4.1.3). Ill-conditioning is also found in more conventional three dimensional inverse solutions. The problem has been handled, in pressure signature solutions to date, by increasing the element pitch and/or reducing the number of elements when the amplitude of the oscillations becomes too large.

A serious instability problem surfaced recently (1995) in an unpublished study of a non-planar, unpowered system that was located above the tunnel centreline. Having generated synthetic signatures using a theoretical vortex-source model with twenty elements at ten locations, it was found to be impossible to recover the original element strengths from the signatures because of extreme oscillations. In some instances, these oscillations propagated to the interference solution. This prompted the development of a solver that detects columns in the influence matrix that are "nearly-dependent" and

eliminates the redundant ones. Row reduction is also possible. With a suitably chosen "near-dependency" parameter, the element distribution is thinned and the matrix ill conditioning (solution oscillation) is reduced to an acceptable level. After applying this procedure, the interference distributions closely matched the theoretical ones generated by the original elements. This new approach could be called 'quasi-linear' because it edits out redundant elements from the original set. The overall effect is to select optimum element locations on a piecewise basis rather than the continuous basis of a true non-linear solution.

Further comments on the construction of the theoretical model are given in Section 4.2.6.

### 8.3.1.5 THE WAKE-INDUCED DRAG INCREMENT

The tunnel-induced drag on the source-source-sink model of Figure 8.18 was analysed first by Hackett et al [12] and later by Cooper, Hackett, Wilsden et al [2] and by Hackett [18], [19], who showed that the in-tunnel wind-axis drag coefficient exceeds the free air value by

$$DC_{Dvis} = \frac{1}{2}\left(\frac{Q_W}{U_\infty A_{TUN}}\right) C_{Dvis}$$

where $C_{D_{vis}}$ is the viscous part of the model drag coefficient and the symbols inside the brackets are as defined previously. $\Delta C_{D_{vis}}$ is subtracted from the measured drag coefficient prior to applying the dynamic pressure correction.

The ½( ) term is the tunnel-induced interference velocity at the wake source location, due to wake source interference, which is proportional to $Q_W$. This acts on a source that represents the model viscous drag. The two source values are different because $Q_W$ , which is obtained from the wall signature, includes wall boundary layer effects whereas the source representing model drag does not. If $C_{D_{vis}}$ Is not readily available, Cooper et al [2] suggest that a value derived from $Q_W$ should be used instead. Conversely, a $C_{D_{vis}}$ based source strength is suggested if $Q_W$ is unavailable. An example of the latter type is given in Section 8.2.3 of this report. The $C_{D_{vis}}$ based approximation will underestimate the correction while the $Q_W$ based approximation will overestimate it. If the wall boundary layers are disturbed significantly by the model, as in car testing for example, the differences between these alternatives can be substantial.

Hackett [18], [19] discusses the flow physics implied by the above correction for a normal flat plate. He suggests, with some experimental support, that the added drag in the wind tunnel reflects a change in separation bubble shape caused by tunnel-induced velocity gradients. Both these references and Cooper et al [2] show, however, that this is *not* horizontal buoyancy as usually calculated from the product of static pressure gradient and model volume. Rather, it is shown by kinematic arguments that, when a full analysis of the system is conducted, the gradient-volume term cancels with another.

## 8.3.2 EXPERIMENTAL ASPECTS

### 8.3.2.1 TESTING AND PRE-ANALYSIS

Pressure instrumentation is installed along the centrelines of the tunnel roof, floor and walls with sufficient length to capture the upstream and downstream asymptotes (Figure 8.18) and sufficient resolution in the vicinity of the model to define the suction and pressure peaks properly. For aeronautical applications, this usually means that the full test section length must be covered, with about twenty orifices for each of the four signatures. The subject of orifice distribution within the test section length is discussed in Section 4.2.5. Hackett et al [11] give details of the layout used for the knee-blown flapped wing tests quoted in Section 8.1.

It is not unusual for a test section to be too short and special procedures may be needed to estimate the upstream and downstream asymptotes. Cooper, Hackett, Wilsden et al [2] describe an iterative procedure that is used to estimate the downstream asymptote and make appropriate adjustments. Situations with too-short an upstream test length should be avoided because the tunnel reference system may be compromised. However, it is demonstrated in Wilsden [43] that, with careful pressure signature analysis, even this situation is recoverable. A source of suitable strength is placed far upstream to shift the signature vertically and thereby correct the front asymptote. Good asymptotes will be assumed in the discussion below.

Real wind tunnel walls and pressure orifices may, in practice, be imperfect. For this reason, and because of the sensitivity of the method to measurement errors, it is important to acquire a reference set of pressures with the model removed from the test section ("empty tunnel signature"). These reference data, converted to velocities, are subtracted from the corresponding model-present data. In certain cases 'empty' tunnel data may be taken with model mounts or a sting installed. Flow calibration at the model position must, of course, be carried out with the same equipment in place. Furthermore, if the presence of the model imposes a significant supervelocity at the wall, the 'empty' reference velocities must themselves be corrected before subtraction. Thus the simple superposition equation:

$$\left[\frac{u}{U}\right]_{CORR} = \left(1 + \left[\frac{u}{U}\right]_{MEAS}\right) - \left(1 + \left[\frac{u}{U}\right]_{EMPTY}\right)$$

becomes, on correcting the empty tunnel data:

$$\left[\frac{u}{U}\right]_{CORR} = \left(1 + \left[\frac{u}{U}\right]_{MEAS}\right) - \left(1 + \left[\frac{u}{U}\right]_{EMPTY}\left(1 + \left[\frac{u}{U}\right]_{MEAS}\right)\right)$$

Only sidewall pressures are needed to determine the blockage for a centrally-mounted, vertically-lifting model. The lifting system generates mainly upwash at the sidewalls and this affects the pressures only at very high lift (see Section 8.3.4). In principle, a blockage signature can be obtained for a lifting model by calculating the mean of the roof and floor velocity signatures, thereby eliminating the lifting circulation. However there is no strong reason to do this (and there are often good reasons not to) so the necessary working charts (see below) have never been prepared.

#### 8.3.2.2 SPECIAL INSTRUMENTATION CONFIGURATIONS.

A reduction from the full, four-wall pressure instrumentation is possible in some situations. As already indicated, only sidewall pressures are needed if the model is centred in the tunnel and conventional angle-of-attack corrections are to be used. Both sidewalls should be instrumented a) to accommodate yawed cases, b) as insurance against small tunnel/model asymmetries in nominally symmetric cases and c) to allow comparison between walls as an aid to troubleshooting.

Only ceiling pressures are needed to determine blockage when testing cars or floor-mounted half-models. The number of orifices can be tailored to approximately a dozen if it is known that model variations will be small. Three-surface instrumentation is sometimes used when tunnel operations preclude floor orifices or under conditions with heavy jet impact at the floor. Pressure signature-based angle-of-attack corrections are possible with this configuration, but lift corrections calculated without the floor signature may be less reliable.

A long test section is beneficial when testing models that are aerodynamically large, mainly to ensure that a good estimate can be made of the downstream asymptote (see below). A good example of this is the fact that, prior to the knee-blown flap model tests described earlier, it was determined that the test section length should be increased from 1.04 B to about 2.0 B. This was, in fact, done (see Hackett et al [11]). The model was situated at a station 0.55 B from the front of the test section. This test section length is not unusual. However, the model is placed further aft in most tunnels, between 0.75 and 1.00 B.

### 8.3.3 ANALYSIS FOR THE "SOURCE-SOURCE-SINK" VERSION OF THE METHOD.

#### 8.3.3.1 BLOCKAGE SIGNATURE ANALYSIS

The object of the initial analysis is to resolve the measured signature into symmetric (solid blockage) and antisymmetric (wake blockage) parts (Figure 8.18). For a simple signature with well defined asymptotes the procedure starts by determining the normalised wake source strength from the asymptotic velocity, $u_{ASYMP}$ (Figure 8.21) using

$$\left(\frac{Q_W}{U_\infty\ A_{TUN}}\right) = \left(\frac{u_{ASYMP}}{U_\infty}\right)$$

which is obtained from considerations of continuity. An initial estimate is then made for $X_2$ , the position of the wake source: the model position is usually selected. The wall signature is then calculated for the wake source acting alone in the wind tunnel, with its tunnel images included. This signature is

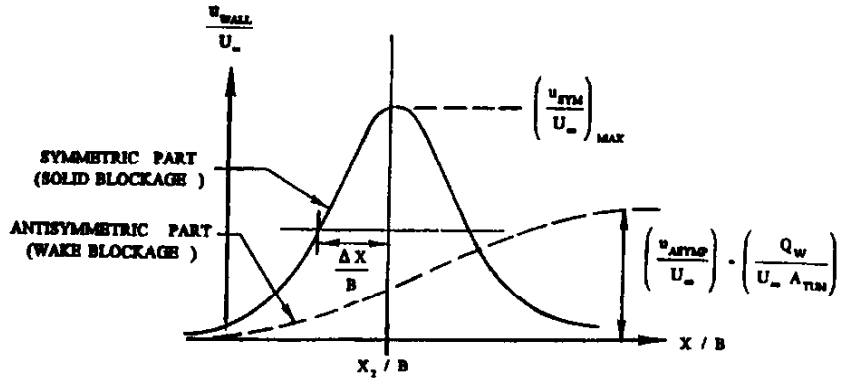


Figure 8.21 Wall pressure signature analysis for the „Source-Source-Sink" version of the pressure signature method

subtracted from the measured data to yield a trial symmetric (solid blockage) signature. Next, the peak of this symmetric part is fitted using a parabola and the location of its apex is determined. If the X-value for the peak coincides with the position selected for $Q_W$ , within a chosen tolerance, then this part of the signature analysis is complete and the flow model can be constructed. If the peak position lies forward or aft of $Q_W$, then the wake source is moved towards it and the process is repeated until the two coincide. The computer code includes the necessary logic to ensure convergence. This establishes $X_2$ (Figure 8.21). The signature analysis phase is completed by determining the height, $(u_{SYM}/U_\infty)_{MAX}$ , of the symmetric part of the signature and then DX, the half-width at half-height.

### 8.3.3.2 Construction of the Source-Source-Sink Theoretical Model

Figure 8.22 shows the procedure for constructing the source-source-sink flow model. The quantities found from the analysis given above appear in the second row of the chart. The wake source analysis, which is already done, appears as the right hand column. The remainder of the chart shows how $Q_S$ and $c_S$, the remaining components of the blockage model (Figure 8.18), are determined.

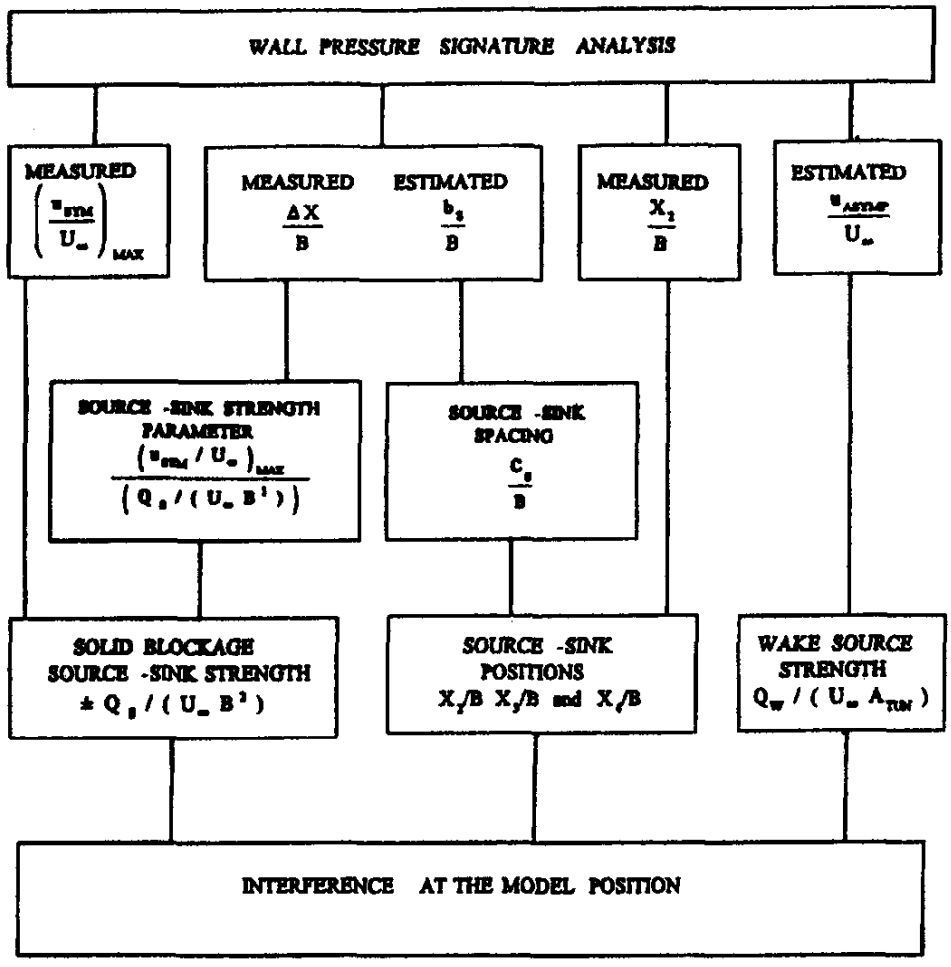


Figure 8.22 Flow Chart for the „Source-Source-Sink" version of the pressure signature method

Figure 8.23 shows the source-sink strength parameter as a function of the peak semi-width DX / B for a range of source span $b_S$ /B. The value of $(u_{SYM} / U_\infty)/(Q_S / U_* B^2)$ , obtained from this plot, is divided into the measured value of $(u_{SYM} / U_\infty)$ to yield the normalised source-sink strength $(Q_S / U_\infty B^2)$.

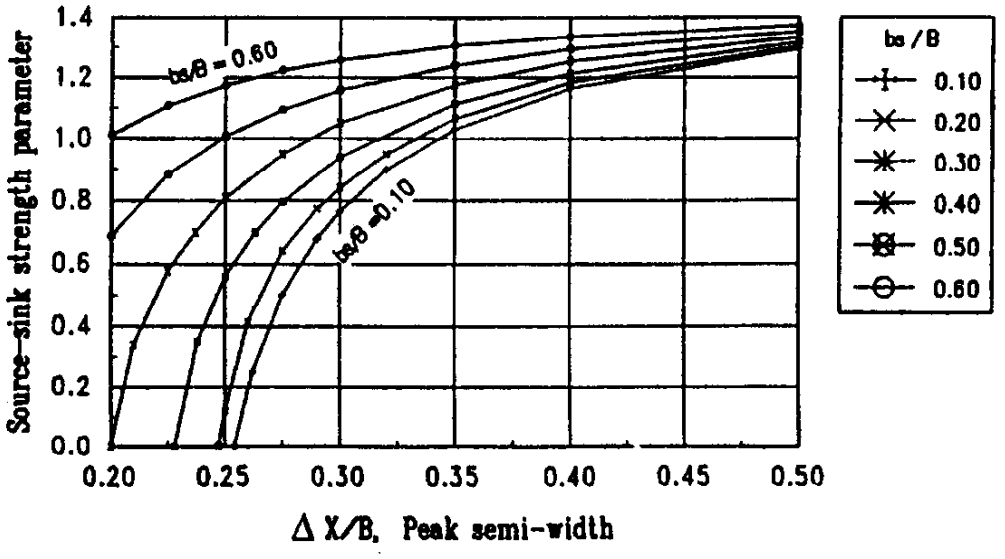


Figure 8.23 Source-sink strength parameter $[(U_{SYM}/U_\infty)/(Q_S/U_\infty B^2)]_{MAX}$ as a function of source-sink span and peak semi-width for H/B = 0.707

Figure 8.24, which has the same general layout as Figure 8.23, is used to determine the source-sink spacing $c_S$ / B. $X_3$ / B and $X_4$ / B are then determined as ($X_2$ / B) ± ½ ($c_S$ / B). This completes the definition of the source-source-sink model.

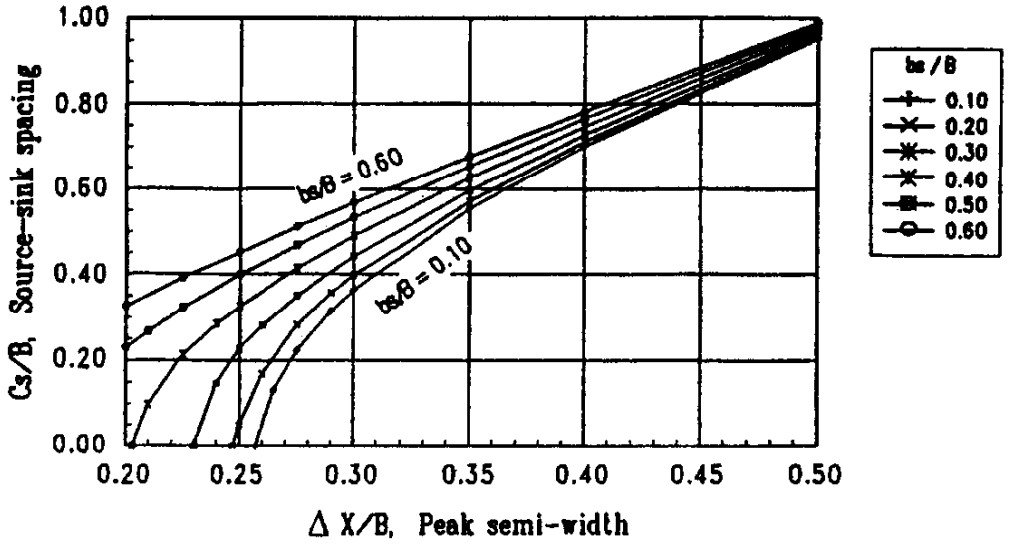


Figure 8.24 Source-sink spacing as a function of source-sink span $b_S$/B and peak semi-width for tunnel H/B = 0.707

### 8.3.3.3 APPLICATION OF THE SOURCE-SOURCE-SINK MODEL.

With the strengths, spans and locations of two sources and a sink now known, tunnel blockage is determined by superposing the image effects of each of these, using the generic interference curve of Figure 8.25. It will be noticed that the curve is essentially independent of $b_S$ / B. The fact that the curve asymptotes to 1.414 ( = B / H), rather than 1.00, is a consequence of employing $B^2$ in the normalisation, rather than BH. This is a carry-over from early versions of the method. Finally, the contributions of the three singularities, with suitable X-shifts, are summed to give the blockage velocity distribution along the tunnel centreline. This is now available for tunnel-q correction at the model reference point or at other significant points along a model such as for $C_P$ corrections distributed along the model length. Figure 8.26, taken from Hackett [17], shows drag correlations for a family of four aspect-ratio 3.0 flat plate wings. Their sizes range from 1.6% to 16.7% of the test section area. Broken lines show the uncorrected $C_D$'s. Despite the very large corrections for the 16.7% plate, these data collapse well. Numerous additional examples may be found in Hackett [17] and earlier publications. Hackett, Wilsden and Lilley [12] provide FORTRAN code for this method, including iteration to allow for truncation of the forward and aft asymptotes. A methodology for preparing the charts (or their table equivalents) is also given.

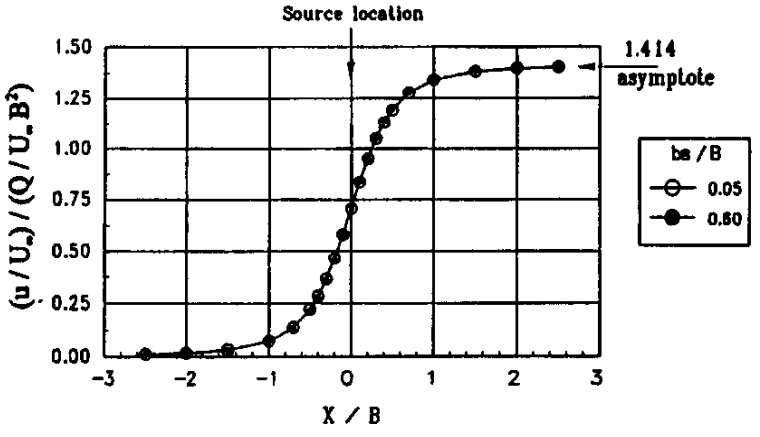


Figure 8.25 Generic curve for determining axial flow interference velocity for a source in a tunnel with H/B = 0.707

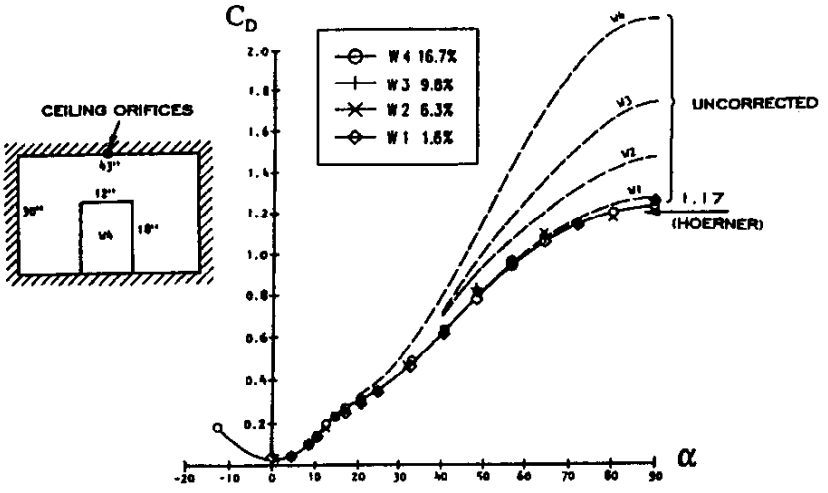


Figure 8.26 Drag correlation for a family of aspect-ratio three flat-plate wings

### 8.3.4 ANALYSIS FOR THE "MATRIX" VERSION OF THE METHOD.

As explained previously, the need for a matrix procedure arises for three main reasons. First, it is faster and more direct than the source-source-sink approach, just described. Second, it has greater geometric flexibility for unusual model shapes. Third, it is better suited to handle the "cross" effects between lift constraint and blockage, discussed in Section 8.3.1 and described in detail below.

#### 8.3.4.1 LIFT-BLOCKAGE COUPLING

The effects of tunnel blockage are felt more or less equally on all four tunnel surfaces. The effects of vertical lift, being antisymetric, are felt mainly at the floor and roof, particularly for unswept wing models. It follows that, as a first approximation, lift effects may be captured by finding the difference between the roof and floor signatures and blockage effects are characterised mainly by the wall signatures. However, these approximations start to break down for swept wings at angle of attack and in very high lift situations in which vortex-induced upwash, at the tunnel walls, is sufficient to influence the pressure measurements there. This is examined in detail in Hackett et al [15]. Nonetheless the above approximations provide a useful basis for a correction procedure.

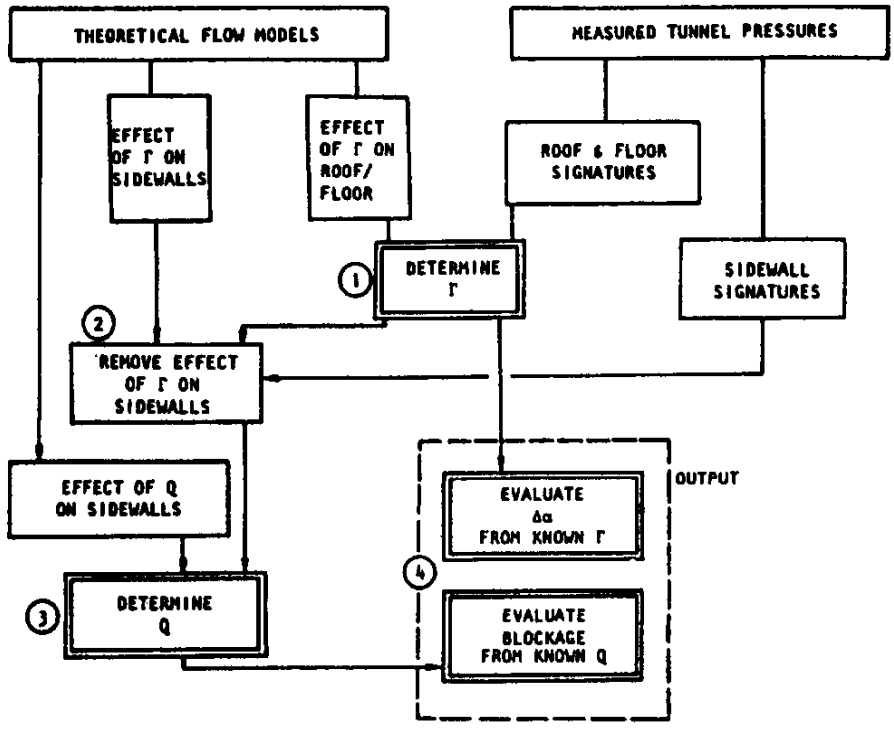


Figure 8.27 Flow chart for the „Matrix" version of the pressure signature method

Figure 8.27, taken from Hackett [17], shows the flow diagram for the matrix version of the pressure signature method. The theoretical part of the procedure involves setting up influence matrices for the effects, at the tunnel walls, floor and roof of the source and vortex arrays that represent the model (see Figure 8.20). Examples of these matrices are given in Hackett et al [14]. The lifting signatures are analysed first (① in Figure 8.27) from which angle of attack corrections may be immediately calculated. The upwash is then calculated at the sidewalls, assuming the trailing vortices to be horizontal, and appropriate corrections are made to the sidewall pressures (see ②). The sidewall data are now ready for

use, and the blockage influence matrix is used to determine the source strength distribution (see ③). Finally, the blockage due to the source images is determined, at ④. A single pass through the procedure is usually sufficient for all but the most extreme cases. Hackett et al [15] describe a corresponding multi-pass procedure and include the necessary FORTRAN code.

### 8.3.4.2 ANGLE-OF -ATTACK CORRECTIONS

It is shown in Hackett [15] that, when applied to simple wings, the angle of attack corrections obtained using the above method agree well with those using conventional methods (e.g. Glauert [3]). The cross-effect corrections were negligible in these cases. For powered models lifting more strongly, the Williams and Butler [44] approach, derived for jet-flapped wings, has been preferred in the past. In this method, the classical Glauert result is divided by ( 1 + (2 $C_\mu$ / $\pi$AR) ). Figure 8.28 shows angle of attack corrections for a swept wing with a knee-blown flap that was tested to very high lift by Hackett et al [15]. Glauert corrections are given by the straight line through the origin; the Williams and Butler corrections are given by the short, inclined lines. These are located appropriately for the $C_\mu$ value concerned. Angle of attack corrections derived from wall pressures are denoted by lines with cross symbols. Successive crosses on a given line represent increasing angle of attack. Both the Glauert and Williams and Butler methods overestimate the low-alpha corrections but severely underestimate the rate of increase with $C_L$, particularly at high-$C_\mu$. This suggests that the corrected lift curve slopes will be lower for pressure signature corrected data than when other correction formulations are used.

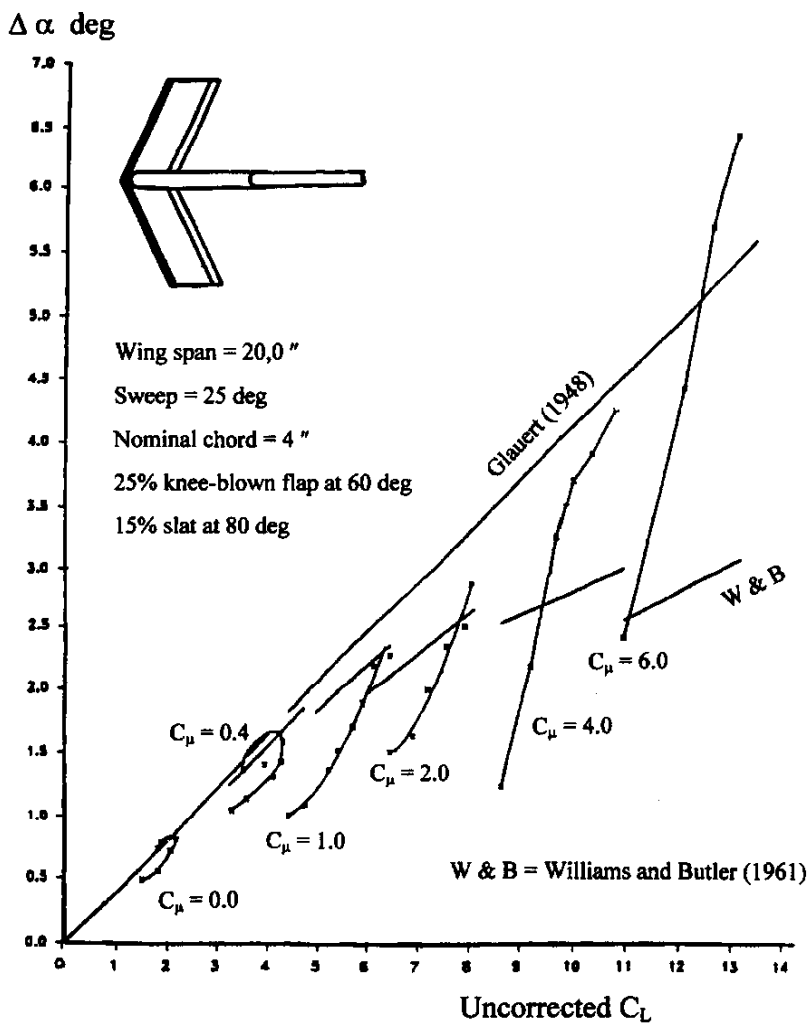


Figure 8.28 Angle of attack corrections for a jet-flapped wing determined by pressure signature and other methods.

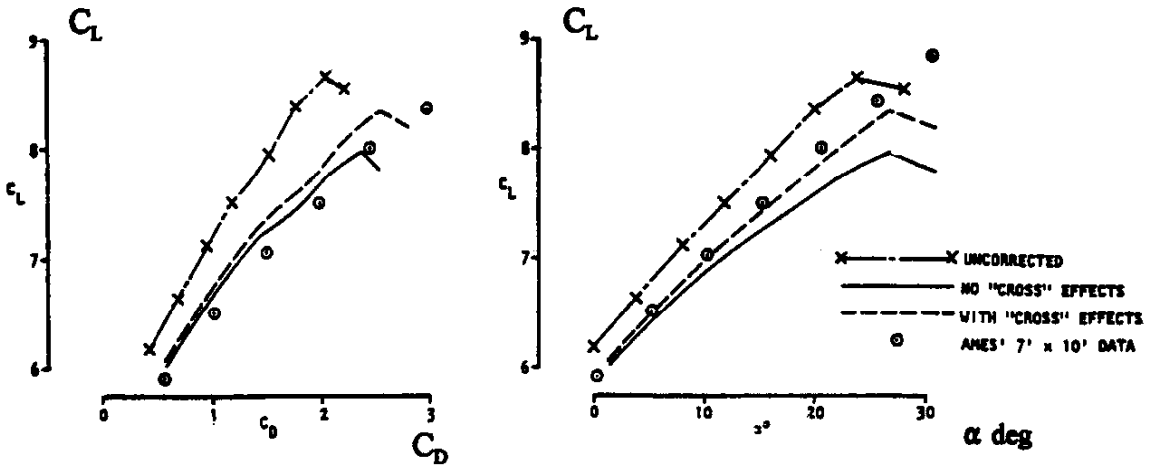


Figure 8.29 Sensitivity of corrections to upwash at the sidewall measuring points.
(Swept, knee-blown flap model at $C\mu = 2.0$)

Figure 8.29 shows the effects of the lift-related sidewall pressure corrections for the $C_\mu = 2.0$ case of the previous figure. Uncorrected data are shown by crosses. Corrected data without wall cross flow effects are denoted by full lines and fully-corrected data have broken lines. These are compared with large-tunnel measurements on the same model, shown by circle-points. Both blockage and angle of attack effects are included. It is apparent that the lift curve is seriously over corrected if the wall cross flow effects are not included. The wall cross flow effects on drag are small, but they shift the curve in the wrong direction relative to the large-tunnel data.

The point is made, in Hackett et al [15], that the present wall cross flow terms can be in error because the vortex trajectory is "frozen" i.e., increases in vortex deflection, with increasing lift, are not accounted for. This is important because the upwash distribution on the wall opposite to a nearby vortex is peaky. This results in underestimation of the wall cross flow effects at low $C_\mu$ and overestimation at high $C_\mu$ . A wake relaxation procedure would remove this difficulty.

### 8.3.4.3 Powered Applications at Very High Lift

Extensive two-tunnel comparisons were made in the late 1970's for a range of knee-blown flap configurations. Two basic models were tested in the (then) Lockheed-Georgia 30 x 42-inch tunnel and the NASA/AAMRDL 7 x 10-foot tunnel. Both models had flapped spans of 20 inches with a nominal chord of 4.0 inches. The flap upper surface angles were 76-degrees and 60.0-degrees for the straight and swept models respectively. Slats were fitted to both models routinely, but these could be removed. 5.0-inch chord tip extensions could be added to both models, bringing their spans to 30-inches. Further details of the unswept and swept models are shown in Figures 8.8 and 8.28.

Sample results will be presented here for the swept-wing configuration with tips and slats fitted. The source references for this and other configurations are:

| | |
|---|---|
| NASA CR 114,496 (Hackett et al [6]) | Straight winged model section design. |
| NASA CR 137,857 (Hackett et al [9]) | Straight winged model test. |
| NASA CR 152,032 (Hackett et al [13]) | Straight and swept model tests. |
| NASA CR 166,186 (Hackett et al [15]) | Straight and swept model tests. |

The above references include a number of configuration variations and various developmental versions of the pressure signature method. Of these, the last reference should be considered definitive because it employs the matrix method, which is better suited to "difficult" pressure signatures.

Figure 8.30 shows the lift and drag characteristics for the swept knee-blown flap model, tested in small and large tunnels, with the tips fitted. Ground blowing was employed as needed. The broken lines show data from the NASA/AAMRDL 7 x10-foot tunnel, the full lines with points are corrected 30 x 43-inch tunnel data. The tunnel corrections were of similar magnitude to those shown in Figure 8.7, for the straight wing. Heavy ground impingement for the upper three curves ($C_\mu$ 's of 4.0, 6.0 and 10.0) rendered the floor pressure signatures unusable and the lifting solutions were obtained using a 'roof-only' program option. The sidewall lift-on-blockage corrections were found to be excessive in these cases and were omitted. These analysis difficulties could probably have been alleviated by a wake relaxation procedure, as mentioned earlier. Such a procedure would deflect the trailing vortices downward in these cases, away from the sidewall pressure orifices.

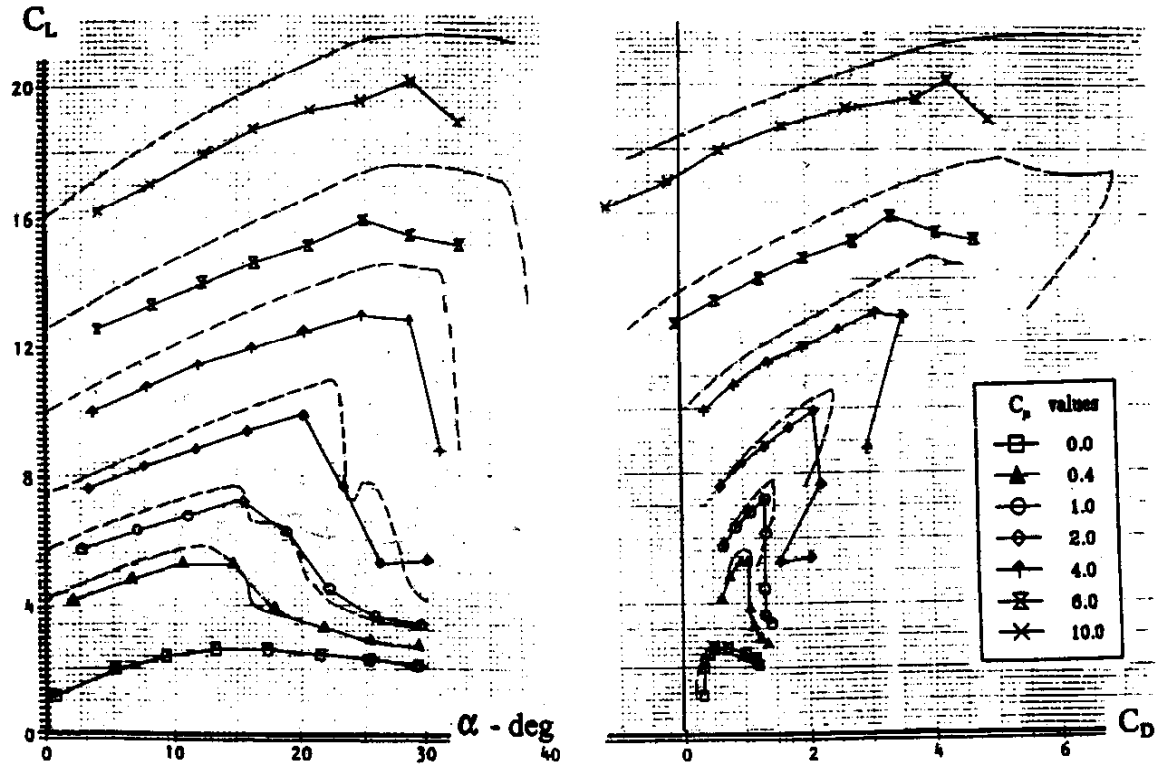


Figure 8.30 Large tunnel and corrected small tunnel lift and drag characteristics for a swept-wing, knee-blown flap model (Large tunnel : broken lines. Small tunnel : symbols

Figure 8.30 demonstrates tendencies towards overcorrection and slightly early stall in the small tunnel that increase at the higher $C_\mu$ 's. Pitching moment characteristics, versus angle-of-attack, were well reproduced in the small tunnel with slightly reduced slopes at the highest $C_\mu$ 's (see Hackett et al [15]). By design, the lift range of Figure 8.30 and for the other configurations quoted above, is probably twice that that is likely to be used in practice. Even with moderate jet impact at the ground and despite the need for large boundary corrections to the small tunnel data, the use of ground blowing and "matrix" pressure signature corrections yields results in the one-to-ten $C_L$ range that reproduce large tunnel data well.

### 8.3.5 Discussion

The source-source-sink and matrix versions of the pressure signature method each have their own advantages and disadvantages. If pressure signature-based angle-of-attack corrections are required, the matrix method must be used because no code has been written for vortex elements comparable to the source-source-sink approach. Other reasons for using the matrix method include its greater geometric flexibility, the fact that an upstream source can be used to deal with asymptote problems at the front of a measured pressure signature and the fact that the method is better suited to batch processing. Balanced against these is the fact that, with too-close element spacing or noisy signature data, the matrix method can generate oscillations in singularity strength that may propagate into the interference distribution. The net wake source strength, used to estimate the wake-induced drag increment (Section 8.3.1), is much less accurate for the matrix method because it is the net of distributed values that may be oscillating. Both methods are susceptible to data scatter in the body of the signature and particular care is needed with the forward and aft asymptotes in both cases. A continued commitment is needed to make wall pressure signature software more self-tending in this regard, including intelligent system health monitoring. The design of the singularity model for the matrix method is still somewhat of an art and a certain amount of cut-and-try is needed to counter excessive oscillations when these are encountered. Work is in progress (Winter 1996) that addresses the latter problem.

## 8.4 Tunnel Interference for a Jet-in-Crossflow

### 8.4.1 Introduction

Whether jet, fan or rotor powered, the defining flow for VTOL aircraft is a round jet directed at right angles to the mainstream. Figure 8.31, taken from Hackett et al [4], shows how a jet emergent from a tunnel floor, for example, is bent by the mainstream towards the streamwise direction. A trailing vortex pair forms and the jet fluid splits into two parts. An equivalent theoretical model, used for estimating tunnel interference effects, will be described below.

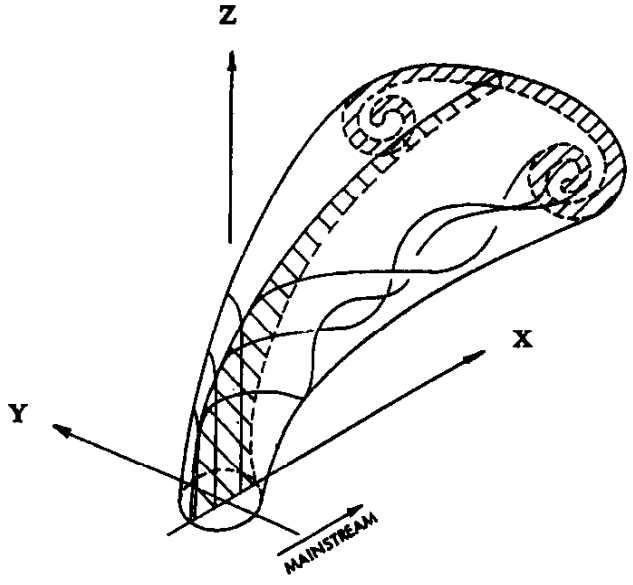


Figure 8.31 Sketch of jet deformation by a crossflow

There is little hope of solving for the details of a jet-in-crossflow theoretical flow model using the methods of Section 8.3: the details are too complex and the three-dimensional inverse process is too fragile. The procedure adopted therefore starts by modelling just the jet and finding its tunnel effects when acting alone. Next, the jet-in-crossflow wall signatures are removed from the measured signatures using the appropriate velocity superpositions. The resulting 'rest-of-model' signatures are then processed using standard pressure signature methods to find *that* part of the tunnel interference. The jet-in-crossflow and 'rest-of-model' interference effects are then added together to give the total tunnel interference.

## 8.4.2 THEORETICAL FLOW MODEL

Figure 8.32 shows the 'skeleton' of vortex, source and doublet lines that comprise the theoretical flow model developed by Hackett et al in 1981. The x-dimension has been foreshortened in this figure. The model recognises the possibility that, in a tunnel test situation, the jet will impinge on the opposite surface of the tunnel - the tunnel roof in the case shown.

The model details were derived using a combination of empirical fits to jet shape with simple jet mixing concepts. Three singularity types are employed in the theoretical model, each with its own specific task. These comprised vortex, source and doublet lines and the result was named the "VSD" flow model. The trajectory and strengths of the vortex model reproduce experimental measurements. The path of the source and doublet lines models the trajectory of the maximum total pressure point in measured jets; this penetrates more deeply into the flow than do the vortices. Source strength is derived from considerations of jet width, combined with simple mixing concepts to accommodate jet growth. The doublet lines provide the appropriate level of wake closure. The trajectory equations, derived in Hackett et al [15] are:

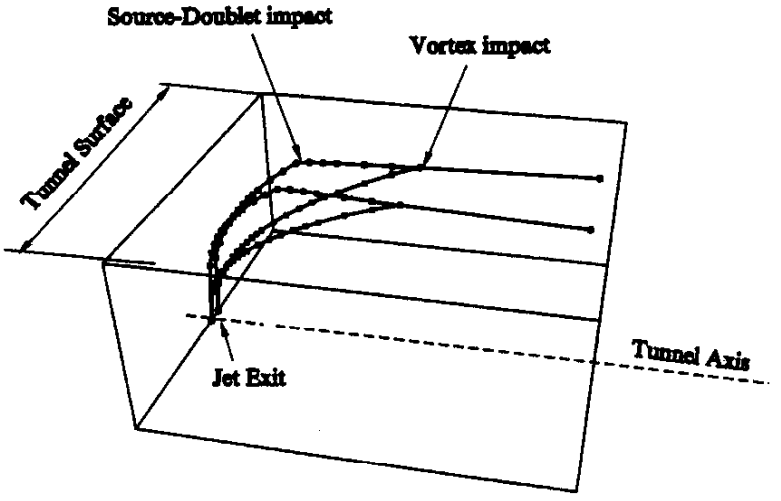


Figure 8.32 Geometry of the jet-in-crossflow theoretical model

$$\frac{Z}{D} = 0.352\left[\frac{X}{D}\right]^{0.429} R^{1.122}$$ , for the vortex pair

$$\frac{Z}{D} = 0.758\left[\frac{X}{D}\right]^{0.333} R^{1.000}$$ , for the source and doublet lines

$$\frac{Y}{D} = 0.0769\left[\frac{X}{D}\right]^{0.440} R^{1.000}$$, for all of the trajectories

The corresponding singularity strengths are given by:

$$\frac{G_{12}}{U_\infty D} = 0.600\frac{R^2}{X_{12}/D}\left(1 - e^{-0.035(X_{12}/D)^2}\right) + 0.0865R^2 \tanh(X_{12}/D)$$ (vortex strength)

$$\frac{s_{12}}{U_\infty D} = \frac{(Z_2 - Z_1)}{D s_{12}}\sqrt{(1 + 0.23\ X_{12}/D)}$$ (source strength /unit length)

$$\frac{m_{12}}{U_\infty D^2} = -\frac{p}{2}\sqrt{(1+0.23X_{12}/D} \quad \text{(doublet strength)}$$

where $X_{12}$ is the mean X-position of a link 1:2, for example, $Ds_{12}$ is its total length and R is the jet-to-mainstream velocity ratio[1]. Density-corrected velocities are used for hot or cold jets. Only the x-wise component of the doublet vector is used.

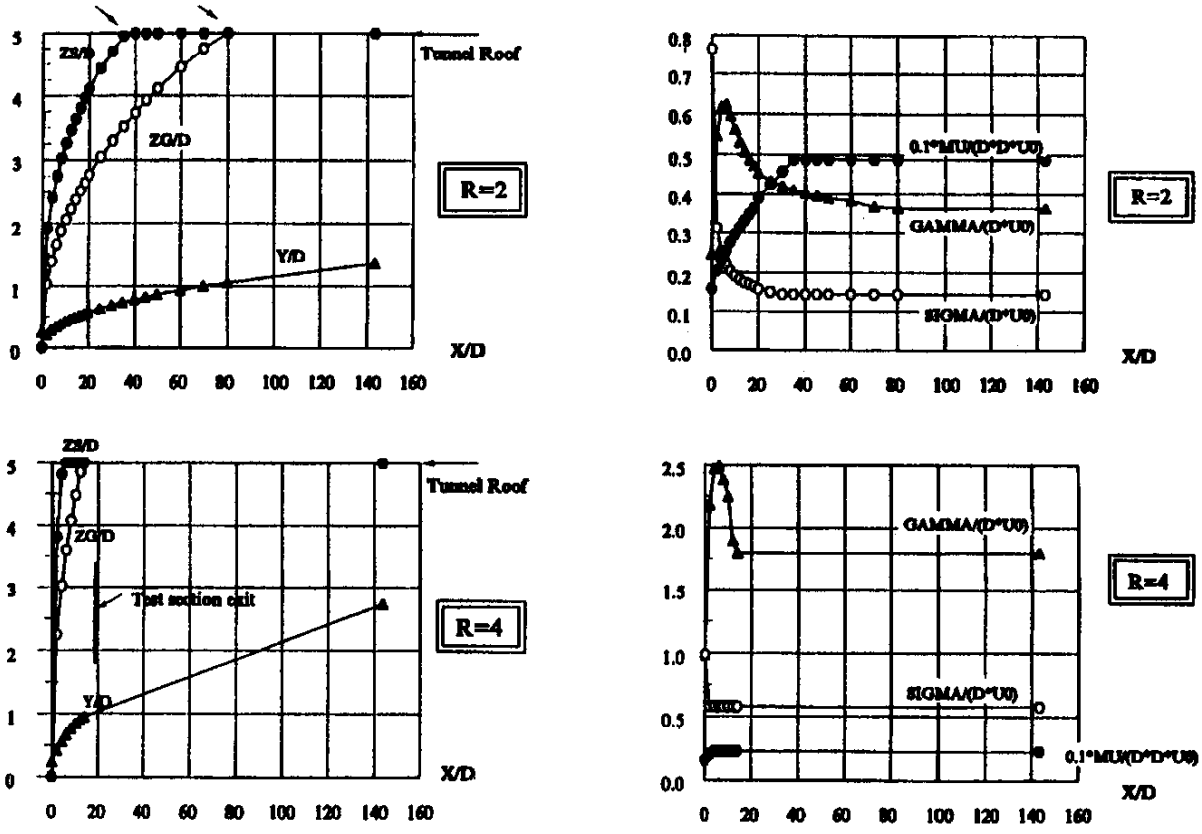


Figure 8.33 Geometry and element strengths for the 3-inch jet at R = 2 and R = 4

Figure 8.33 shows examples of applying the above equations to a 3-inch diameter jet tested in a 30-inch high tunnel. The jet was directed vertically upwards from a pipe whose exit was at mid-height i.e., the jet exit was five jet diameters from the roof and the floor. The test section extended approximately 20-diameters downstream of the jet exit. Data are shown for velocity ratios, R, of two and four. The roof impact occurred downstream of the test section exit for R=2 (left two plots) but fell within the test section at R=4 (right two plots). As already indicated in Figure 8.32, source and doublet impingement occurs before that for the vortex pair. When impact occurs, the vertical motion ceases, horizontal spreading continues and, in the absence of the relevant experimental data, the singularity strengths are 'frozen' at their impact values. The abrupt change in the theoretical plume trajectory at impact raises the issue of whether the real plume bends 'in anticipation' of contact. It was shown experimentally, however, that the jet remains essentially 'stiff' until it is about 1½ diameters from the impingement point.

[1] It should be noted that the final term was omitted from the vortex strength equation of Hackett et al (1981). It was, however, included in the code listing in that document.

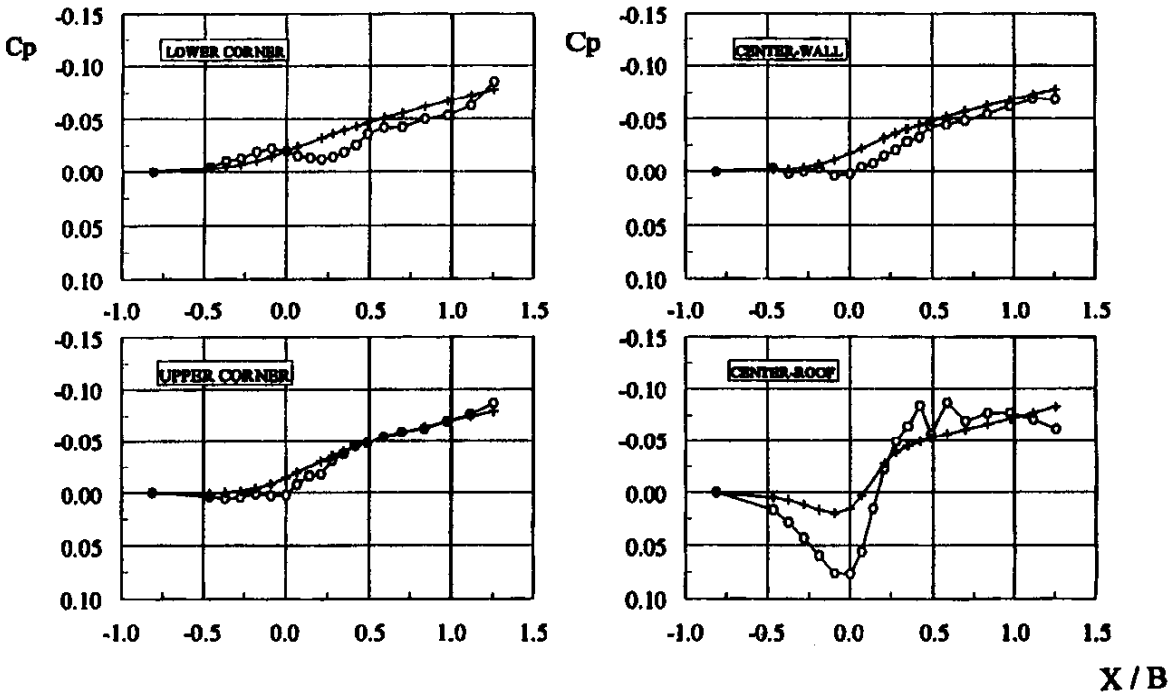


Figure 8.34 Comparison of VSD-model wall pressure preconditions (+) with measurements (o) (3-inch jet at R = 2)

An acid test of any model simulation of the present type concerns its ability to predict wall pressures. The walls are twice as close to the test model as the first tunnel image, so if the wall pressures can be predicted correctly then it is reasonable to assume that the interference predictions are also good. Figure 8.34 shows predicted and measured wall pressures for the R=2 case just described. 'Empty'-tunnel pressures, measured with the jet supply pipe installed, have been removed from the jet-on data using an appropriate superposition procedure. The theoretical model predicts the wall pressures quite well for the tunnel corners and the mid-wall (upper plots and lower left plot in Figure 8.34). However, the positive pressure on the roof ahead of the jet is under-predicted. The reasons are not immediately obvious for the R=2 case. However, for the impinging, R=4 case pressure coefficients greater than plus three were measured on the roof. This reflects higher-than-mainstream total pressures in the jet plume.[2] Upstream propagation of these pressures can be anticipated and it is hypothesised that a similar effect may have been present at R=2, despite the absence of impingement within the test section.

The comparisons quoted above involve a re-implementation of the original code, the electronic version having been lost as a result of various system upgrades. The opportunity was taken to improve the flow model by paying greater attention to detail in the impingement region. The original results show a levelling-out of the predicted pressures towards the end of the test section, rather than the continuously rising characteristics of Figure 8.34. This has been traced to premature plume truncation in the earlier model. The correlations are now significantly better than before for the three-inch jet and somewhat worse for the one-inch jet. However the pressures are much smaller for the one-inch jet ($C_p$'s of order 0.00 to 0.02) and are correspondingly more prone to experimental error when removing the empty tunnel datum pressures. Wall pressures, and by implication the tunnel interference effects, are much greater for the three-inch jet.

---

[2] Simulation of higher-than-mainstream total pressure is beyond the capability of the present theoretical model. A ring-vortex tube model would be required to simulate this condition.

### 8.4.2.1 TUNNEL INTERFERENCE FOR A ROUND JET-IN-CROSSFLOW

As for conventional models, the tunnel interference for jets at low velocity ratio, R, may be calculated using a standard wall image system. However at higher R values, when impingement occurs within the test section length, there is the additional issue of the changed jet shape. Instead of continuing on, the jet is bent suddenly as it hits the tunnel surface and is forced towards the streamwise direction. Changes in the flow field associated with this redirection are part of wind tunnel constraint.

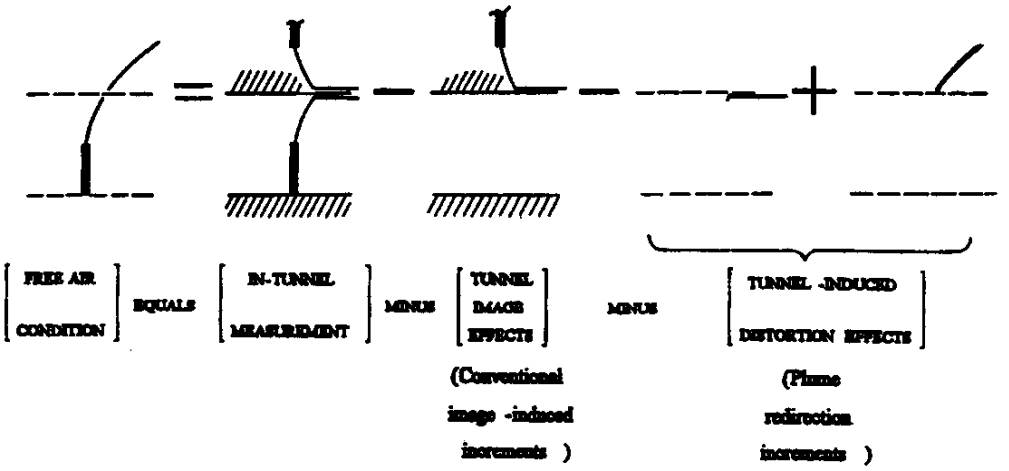


Figure 8.35 Derivation of free air condition from conventional tunnel interference and plume redirection effects

Figure 8.35 shows how this is handled for the present flow model. The desired free air condition, with the plume streaming freely, is built up from three major parts: the in-tunnel measurement; the classical image effect and a plume redirection effect, which has two parts. The first part of redirection removes the deflected part of the plume, within the tunnel, which runs along the tunnel surface. The second part of redirection replaces this by the free-flowing plume extension that would have been present in free air.

Figure 8.36 shows how this works out in practice. The example selected is the R=4 case for the three-inch jet quoted previously. The upper plot shows interference velocities in the mainstream direction. It is found that, at X=0, redirection adds almost 20% to the image-induced interference. The deflected plume at the tunnel surface (lowest curve) provides mainly aft-located source effects that slow the flow at the model location. Removing the roof elements therefore adds to the tunnel induced supervelocity. Adding the extended plume reduces this effect slightly.

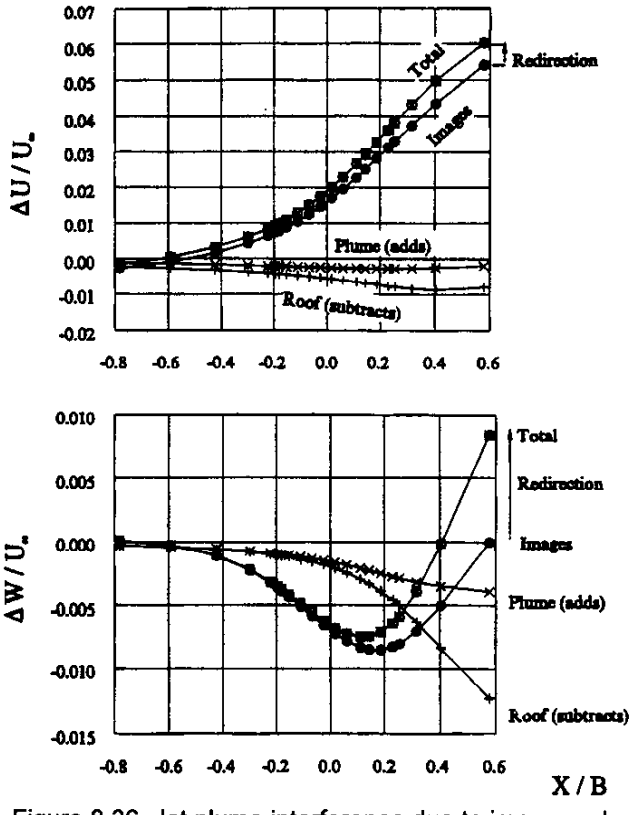


Figure 8.36 Jet plume interference due to image and plume redirection effects. (3-inch jet at R = 4)

The lower plot in Figure 8.36 shows the corresponding effects on upwash interference. The results shown are, of course, for an inverted jet. In this case, redirection *reduces* the interference at X=0 by about 6½%. The redirection effect increases rapidly on proceeding aft, however, so there may be pitching moment implications. Once again the flow mechanism centres around the source links at the roof, which provide significant downwash in the present case (upwash for a downward-directed jet). Removing this adds to the image effect. The extended plume reduces it.

The blockage curves given by Hackett et al [15] flattened out at about X/B = 0.25 whereas the present trend continues upward (upper plot, Figure 8.36). This is attributed to the extension of the present flow model in the impingement region and parallels a similar observation for the pressure signature predictions, discussed earlier. The upwash predictions differ for similar reasons. The present trends now resemble more closely those quoted for other methods.

### 8.4.2.2 Tunnel Interference for Other Configurations

The extension to multiple normal jets is straightforward, since the induced velocities are superposable. However, this covers only one angle of attack/jet deflection angle. The 1981 work was terminated before non-normal jet injection models could be formulated. However, corresponding experiments *were* done for jets directed 30-degrees forward and 30-degrees aft of the vertical. The corresponding flow maps and wall pressure signatures are available in the 1981 reference. These parallel those used to develop the theoretical model described above. It should be possible to model at least these configurations using a similar approach and interpolation for intermediate angles should be straightforward. The fact that the original code required no modification once the basic VSD model was established attests to the soundness of the fluid mechanics that underlie the jet-in-crossflow theoretical model.

For cases with the model in ground effect, no redirection is required, the ground image becomes part of the model and the tunnel image system is modified accordingly. However this option has not been coded into the programme. This approach assumes, of course, that the model is at the appropriate height above the tunnel floor. Ground blowing should be applied at the level for in-ground testing, rather than the level for free air simulation (see Section 8.1.2).

# REFERENCES for CHAPTER 8


[1] Ashill, P.R., Keating, R.F.A., 1988, "Calculation of tunnel wall interference from wall-pressure measurements" The Aeronautical Journal of the Royal Aeronautical Society, January 1988.

[2] Cooper, K.R., Hackett, J.E., Wilsden, D.J. et al, 1995 "Closed test section wind tunnel blockage corrections for road vehicles." SAE Special Publication 1176, May 1995

[3] Glauert, H., 1948, "The elements of airfoil and airscrew theory." Second Edition. Cambridge University Press, 1948.

[4] Hackett, J.E., Miller, H.R., 1971, "A Theoretical investigation of a circular lifting jet in a cross-flowing mainstream." AFFDL-TR-70-170, January 1971.

[5] Hackett, J.E., Praytor, E.B., 1972a, "Ground effect for V/STOL aircraft configurations and its simulation in the wind tunnel: Part I, Introduction and theoretical studies." NASA CR 114, 495. November 1972.

[6] Hackett, J.E., Praytor, E.B., Boles, R.A., 1972b, "Ground effect for V/STOL aircraft configurations and its simulation in the wind tunnel: Part II, Experimental studies" NASA CR 114, 496. November 1972.

[7] Hackett, J.E., Praytor, E.B., Caldwell, E.O., 1972c, "Ground effect for V/STOL aircraft configurations and its simulation in the wind tunnel: Part III, The tangentially-blown ground as an alternative to a moving ground : Application to the NASA-Ames 40- by 80-foot wind tunnel" NASA CR 114, 497, November 1972.

[8] Hackett, J.E., Wilsden, D.J., 1975, "Determination of low speed wake blockage corrections via tunnel wall static pressure measurements." Proceedings of the AGARD Symposium on Wind Tunnel Design and Testing Techniques, Paper 22. See AGARD CP174, October 1975.

[9] Hackett, J.E., Boles, R.A., 1976, "Wake blockage corrections and ground effect testing in closed wind tunnels." Journal of Aircraft, August 1976.

[10] Hackett, J.E., Boles, R.A., Lilley, D.E., 1976 "Ground simulation and tunnel blockage for a jet-flapped, basic STOL model tested to very high lift coefficients." NASA CR 137,857, March 1976.

[11] Hackett, J.E., Boles, R.A., 1977 "Ground simulation and tunnel blockage for a swept, jet-flapped wing tested to very high lift coefficients." NASA CR 152,032. June 1977. (also AIAA 74-641).

[12] Hackett, J.E., Wilsden, Lilley, D.E., 1979, "Estimation of tunnel blockage from wall pressure signatures: a review and data correlation." NASA CR 152, 241, March 1979.

[13] Hackett, J.E., Boles, R.A., 1979c, "Moving ground simulation by tangential blowing." Journal of Aircraft, December 1979 (see also NASA CR 152, 032 and AIAA Paper No.78-814).

[14] Hackett, J.E., Wilsden, D.J., Stevens, W.A., 1980, "A review of the "Wall Pressure Signature" and other constraint correction methods for high angle-of-attack tests." Paper presented to the AGARD Fluid Dynamics Panel, see AGARD Report 692, May 1980.

[15] Hackett, J.E., Sampath, S., Phillips, C.G., 1981a, "Determination of wind tunnel constraint effects by a unified wall pressure signature method: Part I, Applications to winged configurations." NASA CR 166, 186, June 1981.

[16] Hackett, J.E., Sampath, S., Phillips, C.G., White R.B., 1981b, "Determination of wind tunnel constraint effects by a unified wall pressure signature method: Part II Application to jet-in-crossflow cases." NASA CR 166, 187, November 1981.

[17] Hackett, J.E., 1982, "Living with solid-walled wind tunnels." AIAA Paper No. 82-0583, March 1982.

[18] Hackett, J.E., 1994, "Tunnel-induced gradients and their effect upon drag." Lockheed Engineering Report LG83ER0108, September 1994 (Revised from June 1983 ).

[19] Hackett, J.E., 1996, "Tunnel-induced gradients and their effect upon drag." AIAA paper

[20] No 96-0562, January 1996 (Shortened version of Hackett (1994)).

[21] Heyson, Harry H., and Katzoff, S, 1957, "Induced Velocities near a Lifting Rotor with Non-Uniform Disk Loading." NACA Report 1319, 1957.

[22] Heyson, Harry H., 1960, "Jet-Boundary Corrections for Lifting Rotors Centered in Rectangular Wind Tunnels.", NASA TR R-71, 1960.

[23] Heyson, Harry.H, 1961a, "Wind-Tunnel Wall Interference and Ground Effect for VTOL-STOL Aircraft.", J. Amer. Helicopter Soc., vol. 6, no. 1, Jan. 1961, pp. 1-9.

[24] Heyson, Harry H., 1961b, "Nomographic Solution of the Momentum Equation for VTOL-STOL Aircraft." NASA TN D-814, 1961. (Also available as: "V/STOL Momentum Equation", Space/Aeronaut, vol. 38, no. 2, July 1962, pp. B-18 to B-20.)

[25] Heyson, Harry H., 1962, "Linearized Theory of Wind-Tunnel Jet-Boundary Corrections and Ground Effect for VTOL-STOL Aircraft." NASA TR R-124, 1962.

[26] Heyson, Harry H., 1966, "Equations for the Application of Wind-Tunnel Wall Corrections to Pitching Moments Caused by the Tail of an Aircraft Model." NASA TN D-3738, 1966.

[27] Heyson, Harry H., Grunwald, K,J., 1966, "Wind Tunnel Boundary Interference for V/STOL Testing." In NASA SP 116, April 1966, p 409.

[28] Heyson, Harry H., 1969a, "Use of Superposition in Digital Computers to Obtain Wind-Tunnel Interference Factors for Arbitrary Configurations, with Particular Reference to V/STOL Models." NASA TR R-302, 1969.

[29] Heyson, Harry H., 1969b, "Fortran Programs for Calculating Wind-Tunnel Boundary Interference." NASA T X-1740, 1969.

[30] Heyson, Harry H., 1969c, "The Flow throughout a Wind Tunnel containing a Rotor with a Sharply Deflected Wake." Paper presented at the Third CAL/AVLABS Symposium, Buffalo, NY., June 1969.

[31] Heyson, Harry H., 1970, "Theoretical Study of Conditions Limiting V/STOL Testing in Wind Tunnels With Solid Floor." NASA TN D-5819, 1970.

[32] Heyson, Harry H., 1971a, "General Theory of Wall Interference for Static Stability Tests in Closed Rectangular Test Sections and in Ground Effect." NASA TR R-364, 1971.

[33] Heyson, Harry H., 1974, "The Effect of Wind Tunnel Wall Interference on the Performance of a Fan-in-Wing Model." NASA TN D-7518. February 1974.

[34] Heyson, Harry H., 1994, Personal Communication, July 19, 1994.

[35] Margason, Richard J., 1995, Personal Communications, April-July 1995.

[36] Olcott, 1965, " A Survey of V/STOL Wind Tunnel Wall Correction and Test Techniques." Princeton University Report PU 725. (also AD 629 004), December 1965.

[37] Rae, William H., Pope, Alan., 1984, "Low-speed wind tunnel testing", second edition, p 408. Wiley-Interscience, 1984.

[38] Rubbert, P.E., Saaris, G.R., et al, 1967, "A general method for determining the aerodynamic characteristics of fan-in-wing configurations. Volume 1: Theory and application", USAAVLABS Technical Report 67-61A

[39] Rueger, M., Crites, R., Weirich, R., 1995, "Comparison of conventional and emerging ("Measured Variable") wall correction techniques for tactical aircraft in subsonic wind tunnels". AIAA Paper 95-0108, January 1995.

[40] South, P., 1968, "Measurements of flow breakdown in rectangular wind tunnel working sections" NRC Aeronautical Report LR-513. November 1968.

[41] Tyler, R.A., Williamson, R.G., 1970, "Observations of tunnel flow separation induced by an impinging jet" NRC Aeronautical Report LR-537, April 1970.

[42] Tyler, R.A., Williamson, R.G., 1971, "Tunnel flow breakdown from inclined jets", NRC Aeronautical Report LR-545, March 1971.

[43] Wildsen, D.J., 1978, "A low speed wind tunnel test utilizing simple automotive shape (S.A.S.) models at 0.375, 0.475, and full scale in the 16.25 x 23.25 foot test section", Lockheed-Georgia Company Report No LSWT 303, December 1978.

[44] Williams, J. and Butler, S.F.J., 1961, "Experimental Methods for Testing High Lift BLC and Circulation Control Models". See "Boundary Layer and Flow Control.", Volume I, p 390. Lachmann (Ed) Pergamon Press, 1961.